Cavity QED with Rydberg Excitations

LEE CHERN HUI

NATIONAL UNIVERSITY OF SINGAPORE

2014

Cavity QED with Rydberg Excitations

LEE CHERN HUI
B.Sc. (Hons), NUS

A THESIS SUBMITTED

FOR THE DEGREE OF MASTER OF SCIENCE

DEPARTMENT OF PHYSICS
NATIONAL UNIVERSITY OF SINGAPORE

2014

DECLARATION

I hereby declare that this thesis is my original work and it has been written by me in its entirety. I have duly acknowledged all the sources of information which have been used in the thesis.

This thesis has also not been submitted for any degree in any university previously.

.....

Lee Chern Hui

18 August 2014

Acknowledgements

First of all, I would like to thank my supervisor Associate Professor Murray Barrett for giving me the opportunity to work in this wonderful group and for his invaluable input into the project. The fruitful discussions we had have kept me from going down the wrong path and have saved me a lot of time for trial and error.

Next, I would like to extend my gratitude to my mentor and my partner Dr. Kyle Arnold for his guidance ever since I embarked on the project. The progress of the project would not have been possible had it not been for his wealth of knowledge in lasers, electronics and cold atom physics. I am honoured to have learnt from him, for these skills will be the important building blocks of my future career.

Many thanks to Markus Baden, a PhD student of the group for the discussions we had and the many suggestions he provided whenever I am stuck. He also introduced me to the programming language Python which proves to be indispensable in my data analysis and physical modelling.

Last but not least, I would like to thank my fellow mates Arifin, Sandoko Kosen and Raymond Santoso for their endless support and encouragement throughout this endeavour, and of course for the constant reminder of the different deadlines.

Contents

Abstract

We study experimentally the non-linearity of the Jaynes-Cummings model in a multi-atom cavity QED system induced by the presence of Rydberg excitations. ^{87}Rb atoms are trapped in an optical cavity of finesse $\mathcal{F} = 900$ using a red-detuned intracavity optical dipole trap. Rydberg excitations are introduced in the cavity using a two-photon excitation process with a cavity probe beam at 780 nm and a control beam at 480 nm. Preliminary results are obtained such as the observation of the vacuum Rabi splitting and the two-photon Rydberg excitation in free space.

List of Figures

List of Tables

1 Introduction

Quantum Information and Computation (QIC) has received a great deal of attention as it promises much higher efficiency in performing certain classes of tasks as compared to classical computers [1, 2]. A quantum computer, in analogy with a classical one, is made up of information stored in quantum bits (or qubits) and a series of quantum logic gates which act on these qubits to generate the outputs of algorithms. The realization of a large-scale quantum computer would require many qubits. However, the technical difficulty of storing and manipulating many qubits in a single quantum system increases rapidly with their number. One of the proposed solutions to realizing a large-scale quantum computer is the quantum network. A quantum network consists of many quantum nodes that store and process relatively smaller numbers of qubits locally and are linked to each other through quantum channels [3]. In this framework, atomic systems naturally serve as local memory for the storage of information, while photons serve as the information carriers in the quantum channels. Photons are particularly suited as information carriers by virtue of their ease of transport over long distances and their imperviousness to decoherence [1]. Photons are insensitive to decoherence because they normally interact very weakly with other systems and among themselves. While this is advantageous for an information carrier, it makes it difficult to realize the interactions required for quantum logic gates using single photons.

One means of achieving the required interaction strength is to use an optical cavity to mediate the interaction between the photonic and atomic systems. Owing to the high reflectivity of the mirrors that constitute the cavity, the dipole interaction between the atom and the electromagnetic field is significantly enhanced due to the multiple

passes made by a single photon within the resonator. This so-called cavity quantum-electrodynamics (CQED) system is well-described by the Jaynes-Cummings model [4] which predicts a characteristic optical non-linearity at the single photon level. This non-linearity manifest most clearly in the 'photon-blockade' effect whereby after a single photon enters the cavity, subsequent incident photons are reflected. This effect has been experimentally observed [5] and demonstrates the capability for effective photon-photon interactions mediated via the atom-cavity system. Such photon-photon interactions are critical resources for a deterministic optical quantum computer [1], for example enabling the realization of an optical C-NOT gate [6]. Many experiments have used strong coupling between a single atom and photon inside a high-finesse optical cavity to demonstrate the basic processes required for quantum computation [5, 7, 8, 9].

To achieve this so-called 'strong-coupling' regime between a single atom and the cavity field, a cavity of sufficiently high finesse is required. This poses a technological barrier due to the difficulty in cavity manufacture and the sensitivity of these cavities to defects such as birefringence[5]. Furthermore, these experiments are notoriously complex and lossy, limiting their scalability and practical application. One possibility to improve the situation is to instead use an ensemble of N atoms and relax the requirements on the cavity finesse. Having N atoms coupled to a single cavity mode enhances the coupling strength by a factor of $\sqrt{N}$. The downside is that the N-atom system can now absorb multiple excitations, as opposed to the single atom situation, and the non-linear features of the Jaynes-Cummings model are no longer present. So while an ensemble-cavity system benefits from enhanced coupling and low losses, which are useful for some QIC applications such as efficient quantum memories [10] and on-demand photon sources [11], there is limited scope for realizing quantum optical non-linearities in this system.

Aside from strong-coupling optical resonators, another promising means of realizing an strong optical non-linearity is to use the dipole-dipole interaction between Rydberg states. Rydberg states are highly excited atomic states with high principle quantum number (typically $n \gtrsim 20$). Electrons in Rydberg states have orbitals far from the nucleus, resulting in a high polarizability. Although the van Der Waals potential is normally weak and neglected, it scales as n^{11} [12]. Thus Rydberg atoms interact strongly

over relatively long distances ($\sim 10\,\mu\mathrm{m}$) through the van Der Waals potential. Consequently, when a single atom is excited by a laser to a Rydberg state, nearby atoms experience an energy shift which prevents a second atom from excitation to the Rydberg state. This is known as the 'Rydberg-blockade' effect and is clearly analogous to the above mention 'photon-blockade' effect of CQED. The Rydberg-blockade effect has been used to demonstrate strong optical non-linearities in free-space atomic ensembles [13, 14].

The aim of our experiment is to investigate quantum optical non-linearities in a hybrid system consisting of an atomic ensemble in a cavity with Rydberg excitation. While strong absorptive non-linearities have already been observed in an ensemble of Rydberg atoms [22], our system potentially enables a strong quantum non-linearity in the dispersive regime. Ideally, one can consider an ensemble for which a single Rydberg excitation prevents absorption of any further excitations by the entire ensemble. Inside a cavity, this ensemble could be considered as a single 'super-atom' which can only absorb one excitation but has a collectively enhanced coupling to the cavity. This hybrid system can be formally reduced to a Jaynes-Cummings description with an ultra-strong effective coupling [15]. Using state-of-the-art high finesse mirrors, one could realize non-linearities far stronger than previous single-atom cavity experiments. Even using more readily accessible moderate finesse cavity mirrors and ensemble sizes [16, 17], one can reach an interesting quantum non-linear regime. In our first attempt to study this hybrid system, we have opted a build a cavity of only moderate finesse ($F \approx 1000$) to make experiment more technically feasible.

This report summarizes a year-long project which consisted largely of constructing the experimental apparatus and preliminary measurements in preparation of the above experiment. The report is structured as follows: in chapter 2, the theoretical aspects of the project will be presented, including the general results of cavity QED which will subsequently be used in the analysis of our experimental result. The construction of the necessary tools for the experiment and the experimental procedures will be presented in detail in chapter 3. In chapter 4, we analyze the preliminary results and discuss the difficulties encountered. The conclusions and discussion on the future plans for the project

will be presented at the end of the report.

2 Theoretical Foundations

In this chapter, we present the theory upon which the experiment is based. In Sec. 2.1, the general results of multi-atom cavity QED are presented; in Sec. 2.2, we discuss a semiclassical model of cavity transmission for two-level and three-level media; in Sec. 2.3, we first introduce atomic Rydberg states and discuss their properties. Finally, we present a combined Rydberg-cavity QED model and point out its important qualitative features.

2.1 Cavity QED system with N independent atoms

In a system where N two-level atoms are coupled to the same cavity mode and the interaction between atoms is negligible, the system is well described by the Tavis-Cummings Hamiltonian

$$\hat{H} = \hbar\omega_c \hat{a}^\dagger \hat{a} + \hbar\omega_0 \sum_{i=1}^{N} \hat{\sigma}_i^\dagger \hat{\sigma}_i + \hbar \sum_{i=1}^{N} g_i \left(\hat{a}\hat{\sigma}_i^\dagger + \hat{a}^\dagger \hat{\sigma}_i \right) \quad , \tag{2.1}$$

where ω_c is the cavity resonant frequency, ω_0 the atomic transition frequency, g_i the coupling factor between the cavity mode and the i-th atom, $\hat{a}$ the cavity mode annihilation operator and $\hat{\sigma}_i$ the atomic lowering operator of the i-th atom. This Hamiltonian is essentially the sum of the cavity photon energy, atomic energy and the interaction between the two.

The Hamiltonian can be further simplified by defining the collective spin operators

$$\hat{S} = \frac{1}{\sqrt{N}} \sum_{i=1}^{N} \frac{g_i}{\bar{g}} \hat{\sigma}_i \,, \quad \hat{S}^\dagger = \frac{1}{\sqrt{N}} \sum_{i=1}^{N} \frac{g_i}{\bar{g}} \hat{\sigma}_i^\dagger \quad \text{where } \bar{g} = \sqrt{\frac{1}{N} \sum_{i=1}^{N} g_i^2} \tag{2.2}$$

and transforming into the rotating frame using $\hat{U} = \exp\left(i\omega_0 t(\hat{a}^\dagger \hat{a} + \sum_{i=1}^{N} \hat{\sigma_i}^\dagger \hat{\sigma_i})\right)$,

$$\tilde{H} = \hat{U}\hat{H}\hat{U}^\dagger + i\hbar \left(\frac{d}{dt}\hat{U}\right)\hat{U}^\dagger = \hbar\Delta_c \hat{a}^\dagger \hat{a} + \hbar\sqrt{N}\bar{g}\left(\hat{a}\hat{S}^\dagger + \hat{a}^\dagger \hat{S}\right) \tag{2.3}$$

with $\Delta_c = \omega_c - \omega_0$.

In the subspace of low excitation number,

$$\begin{aligned}
\left[\hat{S}, \hat{S}^\dagger\right] &= \frac{1}{N\bar{g}^2} \sum_{i=1}^{N} g_i^2 \left(|\mathrm{g}_i\rangle\langle \mathrm{g}_i| - |\mathrm{e}_i\rangle\langle \mathrm{e}_i|\right) \\
&= \sum_{i=1}^{N} \left(1 - \frac{2g_i^2}{N\bar{g}^2}\right) \left(|\mathrm{g}_i\rangle\langle \mathrm{g}_i| + |\mathrm{e}_i\rangle\langle \mathrm{e}_i|\right) \\
&= \mathbb{1} + O\left(\frac{1}{N}\right)
\end{aligned}$$

Hence, for low excitation and large N, $\hat{S}^\dagger$ ($\hat{S}$) behaves like the raising (lowering) operator of a harmonic oscillator. The atoms-cavity system can thus be considered as two coupled harmonic oscillators of frequency ω_c and ω_0 respectively, with the coupling strength $\sqrt{N}\bar{g}$. It can therefore be seen that the coupling strength of an ensemble of N atoms is enhanced by a factor of $\sqrt{N}$ compared to a single atom. It is easily verified that the ground state of the Hamiltonian (2.1) is $|\mathrm{G}^{(N)}\rangle \otimes |0\rangle$, and the states

$$|+\rangle_1 = \cos\theta_1 |\mathrm{G}^{(N)}\rangle \otimes |1\rangle + \sin\theta_1 |\mathrm{E}^{(N)}\rangle \otimes |0\rangle \tag{2.4a}$$

$$|-\rangle_1 = -\sin\theta_1 |\mathrm{G}^{(N)}\rangle \otimes |1\rangle + \cos\theta_1 |\mathrm{E}^{(N)}\rangle \otimes |0\rangle \tag{2.4b}$$

with the atomic states

$$\begin{cases} |\mathrm{E}^{(N)}\rangle \equiv \frac{1}{\sqrt{N}} \sum_{i=1}^{N} \frac{g_i}{\bar{g}} |\mathrm{g}_1, \mathrm{g}_2, \ldots, \mathrm{g}_{i-1}, \mathrm{e}_i, \mathrm{g}_{i+1}, \ldots, \mathrm{g}_N\rangle \\ |\mathrm{G}^{(N)}\rangle \equiv |\mathrm{g}_1, \mathrm{g}_2, \ldots, \mathrm{g}_N\rangle \end{cases} \tag{2.5}$$

and mixing angles

$$\sin\theta_1 = \frac{\sqrt{4N\bar{g}^2 + \Delta_c\left(\Delta_c - \sqrt{4N\bar{g}^2 + \Delta_c^2}\right)}}{\sqrt{2}\sqrt{4N\bar{g}^2 + \Delta_c^2}} \tag{2.6a}$$

$$\cos\theta_1 = \frac{\sqrt{2}\sqrt{N}\bar{g}}{\sqrt{4N\bar{g}^2 + \Delta_c\left(\Delta_c - \sqrt{4N\bar{g}^2 + \Delta_c^2}\right)}} \tag{2.6b}$$

are eigenstates of the subspace of one excitation, with eigenenergies

$$E_{\pm}^{(1)} = \hbar\frac{\omega_c + \omega_0}{2} \pm \hbar\frac{\sqrt{\Delta_c^2 + 4N\bar{g}^2}}{2}. \tag{2.7}$$

Other eigenstates in this subspace of one excitation are in the form of $|\psi_{\text{atom}}\rangle \otimes |0\rangle$ where

$$|\psi_{\text{atom}}\rangle = \sum_{i=1}^{N} c_i \; |\mathrm{g}_1, \mathrm{g}_2, \ldots, \mathrm{g}_{i-1}, \mathrm{e}_i, \mathrm{g}_{i+1}, \ldots, \mathrm{g}_N\rangle$$

with $\langle\psi_{\text{atom}}|\mathrm{E}^{(N)}\rangle = 0$. These states consist only of atomic excited states and have eigenenergies $\hbar\omega_0$.

When the two individual systems (atoms and cavity) share the same resonant frequency, $\Delta_c = 0$, the resonant frequencies of the composite system are $\omega_c \pm \sqrt{N}\bar{g}$. This splitting in the resonant frequency centered at ω_c is known as the vacuum Rabi splitting and has been observed experimentally even for a single atom in a cavity [5].

2.1.1 Cavity Probing

To experimentally measure the composite system's resonant frequencies, we need to monitor the transmission of a weak probe beam through the cavity. The cavity transmission is proportional to the intracavity field and hence the intracavity photon number $\langle\hat{a}^\dagger\hat{a}\rangle$. Only when the cavity driving frequency ω_p matches one of the eigenfrequencies of the cavity-atoms system does the system respond strongly and cavity transmission is

observed. When the cavity is driven using a weak probe beam of optical frequency ω_p, an additional cavity driving term $\hat{V} = \hbar\eta(\hat{a}e^{-i\omega_p t} + \hat{a}^\dagger e^{i\omega_p t})$ needs to be included to the Hamiltonian (2.1). This driving term couples the ground state to the states $|\pm^{(1)}\rangle$, but not to any other state $|\psi_{\text{atom}}\rangle \otimes |0\rangle$within the same subspace, as can be verified by computing the matrix element $\langle \mathrm{G}^{(N)}, 0|\hat{V}|\psi_{\text{atom}}, 0\rangle$. $|\pm^{(1)}\rangle$ are therefore the only states of interest in the subspace of one excitation.

From the result in Eq. (2.7), we deduce that the resonant frequency of the cavity is shifted from ω_c to $E_\pm^{(1)}/\hbar$. Taken from Ref. [18], Fig. 2.1 is the numerical solution of $\langle \hat{a}^\dagger \hat{a} \rangle$ of the single atom-cavity system, showing the avoided crossing and the resonant frequency shift.

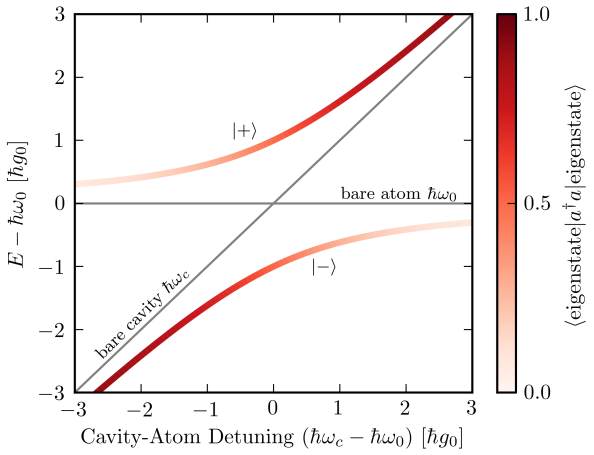

Figure 2.1: Vacuum Rabi splitting for the case of single atom. The splitting is $\sqrt{N}$ times greater for N atoms.

In the case of a single atom coupled to the cavity, if the coupling strength g is sufficiently great such that the resonant frequency shift is resolved by the cavity, the system is prohibited from being doubly excited when driven by a monochromatic source such as a laser, as depicted in Fig. 2.2a for $\Delta_c = 0$. This non-linear effect is called the photon-blockade and has been observed experimentally [5].

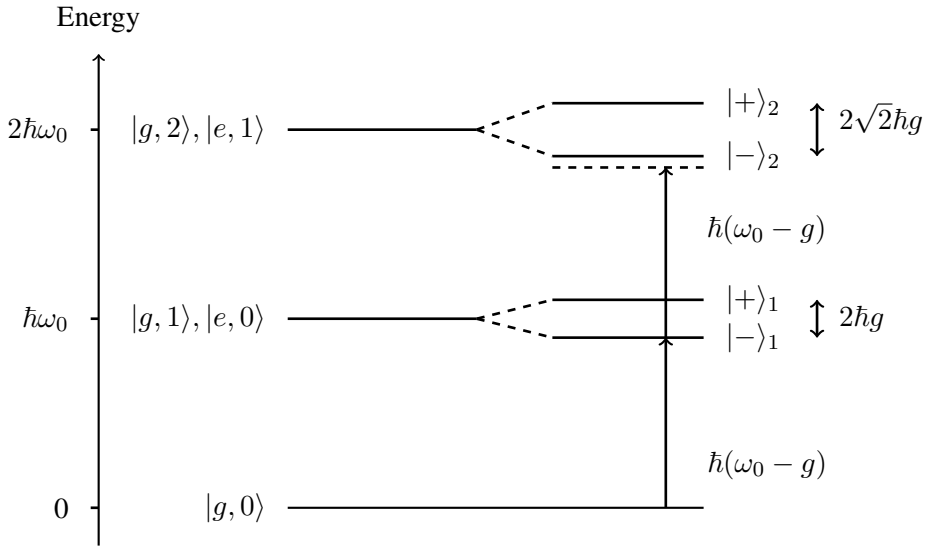

(a) Single atom-cavity system for $\Delta_c = 0$.

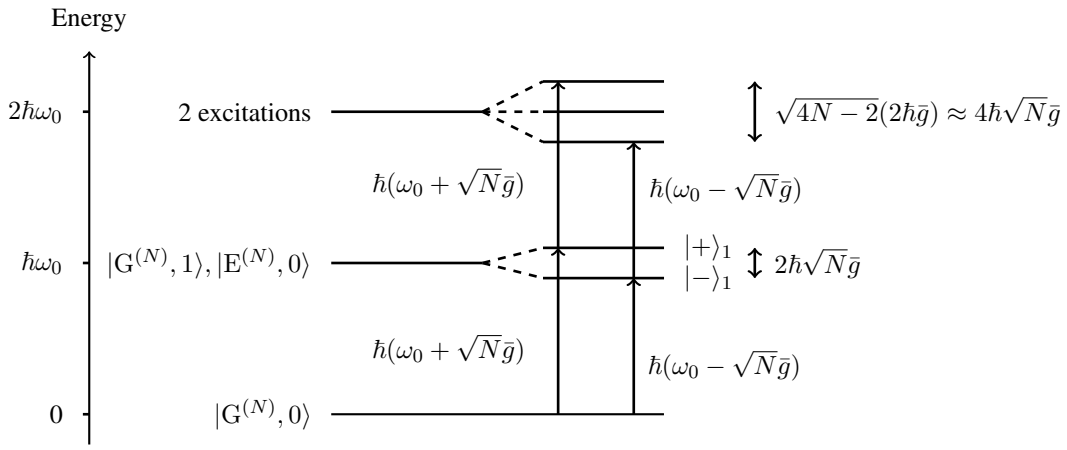

(b) Cavity coupled to $N \gg 1$ atoms for $\Delta_c = 0$.

Figure 2.2: First few energy levels for the (a) single atom and the (b) multi-atom scenarios.

For a cavity coupled to $N \gg 1$ atoms, in the absence of mutual interactions, the atomic ensemble can accept more than one excitation from a monochromatic source and the non-linearity is destroyed as can be seen from Fig. 2.2b. To recover the non-linearity, interactions have to be induced between the atoms, which is where Rydberg excitations come into play as will be detailed in Sec. 2.3.

2.2 Semi-classical Model of Cavity Transmission

In order to model the cavity transmission without solving the full Hamiltonian with the cavity and atomic decay, a semiclassical model is introduced. Given the susceptibility of the intracavity medium, this model computes the steady state intracavity and transmitted field amplitude, taking into account the phase shift and absorption loss due to the medium.

2.2.1 Empty Cavity

Consider an empty cavity formed by mirrors of complex reflectivity r and transmissivity t, with an incident optical field E_{inc} of frequency ω_p. At steady state, the intracavity and transmitted fields are denoted by E_s and E_{out} respectively.

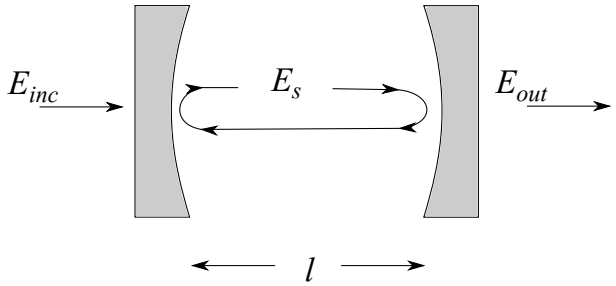

Figure 2.3: Schematic diagram of an empty cavity.

The steady state fields satisfy the relations

$$E_s = r^2 \, E_s \, e^{i\varphi} + t \, E_{\text{inc}} \, , \qquad E_{\text{out}} = t \, E_s$$

where $\varphi = 2k\ell$ is the round-trip phase accumulated by the cavity field. The first relation means that the field folds back on itself after a round-trip, during which the field has been reflected twice; the second relation simply relates the intracavity and the transmit-

ted fields. These give

$$\begin{aligned} E_{\text{out}} &= \frac{t^2\, E_{\text{inc}}}{1 - r^2\, e^{i\varphi}} \\ &= \frac{T\, E_{\text{inc}}}{1 - (1-L)\, e^{i\varphi}} \end{aligned} \tag{2.8}$$

with $T = t^2$ the transmission per mirror, and the loss per mirror $L = 1 - r^2$. The loss L can also be related to κ, the linewidth of the cavity, via $L = \tau\kappa$ where $\tau = 2\ell/c$ is the round-trip time. The empty cavity transmission is defined as

$$T_{\text{empty}} = \left|\frac{E_{\text{out}}}{E_{\text{inc}}}\right|^2 = \frac{T^2}{L^2 + 4(1-L)\sin^2(\varphi/2)} \tag{2.9}$$

When the cavity is on-resonant, φ is a multiple of 2π, and the overall cavity transmission is

$$T_{\text{empty-resonant}} = \frac{T^2}{L^2}. \tag{2.10}$$

Around a resonant frequency ω_c, $\frac{\varphi}{2} = \frac{\omega_c}{c/\ell} + \frac{\omega_p - \omega_c}{c/\ell}$, Eq. (2.9) can be expanded to

$$\begin{aligned} \frac{T^2}{L^2 + 4(1-L)\sin^2(\varphi/2)} &\approx \frac{T^2}{L^2 + 4(1-L)\left(\sin\left(\frac{\omega_c}{c/\ell}\right) + \cos\left(\frac{\omega_c}{c/\ell}\right)\frac{\omega_p-\omega_c}{c/\ell}\right)^2} \\ &= \frac{T^2}{L^2 + 4\pi^2(1-L)\left(\frac{\omega_p-\omega_c}{\omega_{\text{FSR}}}\right)^2} \end{aligned} \tag{2.11}$$

where $\omega_{\text{FSR}} = 2\pi\frac{c}{2\ell}$. This shows a Lorentzian variation with a FWHM of $\frac{2L}{2\pi\sqrt{1-L}}\omega_{\text{FSR}}$ around the resonant frequency. The finesse of the cavity is defined as

$$\mathcal{F} = \frac{\omega_{\text{FSR}}}{\text{FWHM}} = \frac{\pi\sqrt{1-L}}{L} \approx \frac{\pi}{L} \tag{2.12}$$

2.2.2 Cavity with Atomic Medium

Consider now a cavity containing an intracavity atomic medium of resonant frequency ω_0. The medium's response to the intracavity field modifies the cavity transmission

function (2.8) by introducing additional loss and phase shift, which are related by $\chi(\omega_p)$, the steady state susceptibility of the medium [19].

The refractive index of the medium $n(\omega_p)$ is related to the susceptibility via

$$n(\omega_p) = \sqrt{1+\chi(\omega_p)} \approx 1 + \frac{\mathrm{Re}(\chi)}{2} + i\frac{\mathrm{Im}(\chi)}{2}.$$

The round-trip phase and loss are therefore

$$\varphi' = 2k\ell + \mathrm{Re}(\chi)k\ell \tag{2.13a}$$

$$L' = L + (1 - \exp(-\mathrm{Im}(\chi)k\ell)) \approx L + \mathrm{Im}(\chi)k\ell. \tag{2.13b}$$

The normalized (semi-classical) cavity transmission, defined as the ratio of transmitted power to that of an on-resonant empty cavity, is thus

$$\begin{aligned} T_{sc} = \frac{T_{\text{medium}}}{T_{\text{empty-resonant}}} &= \frac{L^2}{L'^2 + 4(1-L')\sin^2(\varphi/2)} \\ &\approx \frac{\kappa^2}{(\Delta_{\text{pc}} + \frac{\omega_p}{2}\mathrm{Re}(\chi))^2 + (\kappa + \frac{\omega_p}{2}\mathrm{Im}(\chi))^2} \\ &= \frac{\kappa^2}{\left|\Delta_{\text{pc}} + i\kappa + \frac{\omega_p}{2}\chi\right|^2} \end{aligned} \tag{2.14}$$

with $\Delta_{\text{pc}} = \omega_p - \omega_c$. This model provides a convenient way to predict the behaviour of the cavity upon probing as exemplified by the following subsections.

Two-level Medium

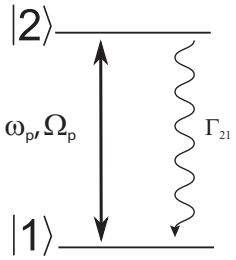

Figure 2.4: Energy diagram of a two-level atom.

For an effective two-level medium driven by a weak probe beam of Rabi frequency Ω_p and a decay rate Γ_{21}, the linear susceptibility is [20]

$$\chi(\omega_p) = \frac{2\rho d^2}{\hbar\epsilon_0}\left(\frac{2\delta_p}{\Gamma_{21}^2 + 4\delta_p^2} - i\frac{\Gamma_{21}}{\Gamma_{21}^2 + 4\delta_p^2}\right)$$

where ρ is the atomic density, d the dipole matrix element of the transition, $\delta_p = \omega_p - \omega_0$ the cavity field detuning from the atomic resonance and ϵ_0 the vacuum's permittivity. For $\Delta_c = \omega_c - \omega_0 = 0$, the cavity transmission peak is split into two, as depicted in Fig. 2.7, in accordance with the vacuum Rabi splitting result Eq. (2.4) for the one excitation manifold.

Three-level Medium

The susceptibility of the medium can be significantly altered with the introduction of a third level using a strong control beam. The third level is usually chosen to have a long lifetime, for example another hyperfine ground state or a metastable state. This level can be introduced in several different ways, but we will focus on the ladder scheme shown in Fig. 2.5c as it is most relevant to our experiment. A comparison of the different schemes can be found in Ref. [21].

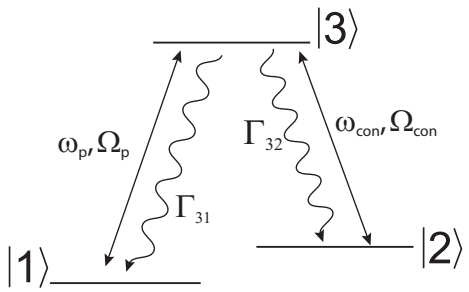

(a) Λ scheme.

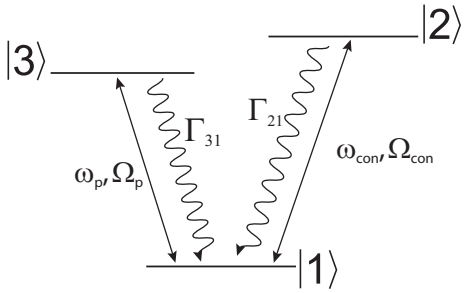

(b) V scheme.

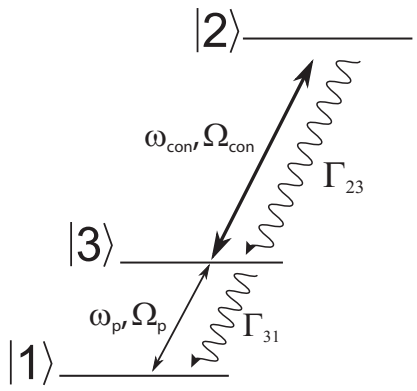

(c) ladder scheme.

Figure 2.5: The different schemes of a three-level system

In all the different schemes, Ω_p denotes the Rabi frequency of the weak probe beam of frequency ω_p, and Ω_{con} denotes that of the strong control beam of frequency ω_{con}. The susceptibility for this system is [22]

$$\begin{aligned}\chi &= \frac{2\rho d_{13}^2}{\hbar\epsilon_0}\frac{i\Gamma_{23} - 2(\delta_{\text{con}} - \delta_p)}{\Gamma_{23}\Gamma_{31} + 4\delta_p(\delta_{\text{con}} - \delta_p) + \Omega_{\text{con}}^2 - i[2\delta_p\Gamma_{23} - 2(\delta_{\text{con}} - \delta_p)\Gamma_{31}]} \\ &= \frac{2\rho d_{13}^2}{\hbar\epsilon_0\Gamma_{31}}\tilde{\chi}\end{aligned} \tag{2.15}$$

with $\omega_{ij} = \omega_i - \omega_j$, $\delta_p = \omega_p - \omega_{31}$, $\delta_{\text{con}} = \omega_{23} - \omega_{\text{con}}$, d_{13} the dipole matrix element between state $|1\rangle$ and $|3\rangle$, Γ_{23} the linewidth of the $|3\rangle \to |2\rangle$ transition.

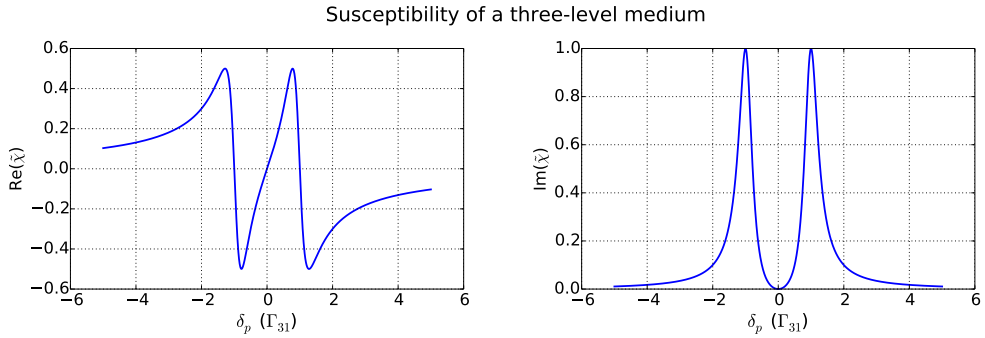

Figure 2.6: Susceptibility of a three-level medium. Plotted for $\Gamma_{23} = 0.0005\ \Gamma_{31}$, $\Omega_{\text{con}} = 2\ \Gamma_{31}$ and $\delta_{\text{con}} = 0$.

The real part of the susceptibility exhibits a change of sign around the two-photon resonance, $\delta_p = \delta_c$, while the imaginary part decreases to well below one. This is the famous Electromagnetically Induced Transparency (EIT) as the absorption of the probe

light by the medium is significantly reduced by using another control beam, creating a transparency window. The cavity transmission is strongly altered due to the modified dispersion of the medium. The transparency window results in the central transmission feature seen in Fig. 2.7. This additional transparency peak has been observed experimentally in Ref. [23] for a three-level medium in the Λ scheme. This transparency window is usually narrower than the cavity and the probe transition linewidths κ and Γ_{31} as shown in the figure, but can be broadened with a stronger control beam.

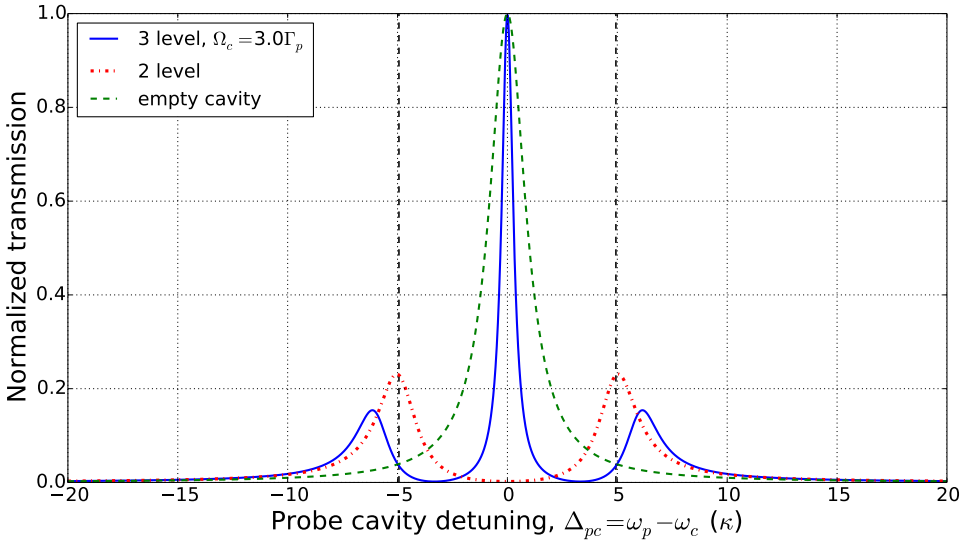

Figure 2.7: Cavity transmission for different media using Eq. (2.14). The horizontal axis is in units of κ, the cavity linewidth. Plotted with the parameters $\kappa = 2\pi \times 2.65\,\text{MHz}$, $\Delta_c = 0$ for $N = 4500$ ^{87}Rb atoms where $|1\rangle = |5S_{1/2}, F = 2, m_F = 2\rangle$, $|2\rangle = |50S_{1/2}, F = 2, m_F = 2\rangle$, $|3\rangle = |5P_{3/2}, F = 3, m_F = 3\rangle$. The two vertical lines denote the position of the vacuum Rabi splitting from Eq. (2.4).

2.3 Rydberg atoms

Dipole-dipole interactions between atoms are only observable when the interatomic separation R is smaller than λ, where λ is the wavelength of the transition [22, 24]. For usual optical transitions, the required density would be $\sim 10^{15}\,\text{cm}^{-3}$, corresponding to an average interatomic distance of $\sim 100\,\text{nm}$. At these densities, the thermal collisions would dominate and preclude the observation of the dipole-dipole interaction,

unless with the use of Bose-Einstein Condensates [25]. This is however not the case for Rydberg atoms.

Rydberg states are atomic states with high principle quantum numbers (usually $n \gtrsim 20$). These states have the properties of [24]

1. long radiative lifetime, for example $\tau \gtrsim 50\,\mu$s for $n \geq 50$ in Rb-87

2. large dipole matrix elements (scale as n^{11}) between energetically close-lying states

3. highly polarizable and very sensitive to electric fields.

Furthermore, the energy separations between neighbouring Rydberg states lie in the millimeter to micrometer wave range. Together with the large dipole matrix element, the length scale for the dipole-dipole interaction is increased from hundreds of nanometer up to a few microns, comparable to the typical interatomic separation in cold atomic samples of moderate density ($10^{10} - 10^{13}$ cm^{-3}).

2.3.1 Rydberg Blockade

Consider a system consisting of two atoms separated by R. Let $|\mathrm{r}\rangle$ be an atomic Rydberg state, and $|\mathrm{r}'\rangle, |\mathrm{r}''\rangle$ two other Rydberg states dipole coupled to $|\mathrm{r}\rangle$. Their relative energy levels are shown in Fig. 2.8. The dipole-dipole potential $V(R)$ between the neighbouring paired Rydberg states scales as $1/R^3$.

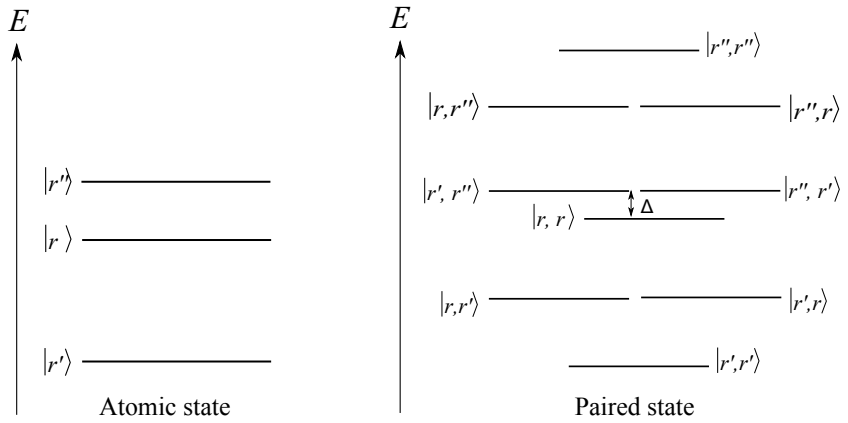

Figure 2.8: Energy levels for the individual Rydberg states $|\mathrm{r}'\rangle, |\mathrm{r}\rangle, |\mathrm{r}''\rangle$ and the paired states. The energy separation between the $|\mathrm{r}, \mathrm{r}\rangle$ state and the $\{|\mathrm{r}', \mathrm{r}''\rangle, |\mathrm{r}'', \mathrm{r}'\rangle\}$ subspace is denoted by Δ.

When the atoms are sufficiently close to each other that the dipole-dipole potential $V(R)$ is comparable to the energy separation Δ between the $|\mathrm{r}, \mathrm{r}\rangle$ state and the states $\{|\mathrm{r}', \mathrm{r}''\rangle, |\mathrm{r}'', \mathrm{r}'\rangle\}$, the Hamiltonian can be solved by diagonalizing it in the subspace of the three coupled paired states [22]. In the subspace spanned by the states $\{|\mathrm{r}, \mathrm{r}\rangle, |\mathrm{r}', \mathrm{r}''\rangle, |\mathrm{r}'', \mathrm{r}'\rangle\}$,

$$\hat{H}_{\{|\mathrm{r,r}\rangle,|\mathrm{r}',\mathrm{r}''\rangle,|\mathrm{r}'',\mathrm{r}'\rangle\}} = \begin{pmatrix} 0 & V(R) & V(R) \\ V(R) & \Delta & 0 \\ V(R) & 0 & \Delta \end{pmatrix}.$$

This Hamiltonian resembles Eq. (2.1) in the one excitation subspace, it admits similar solutions as to Eq. (2.4),

$$\begin{aligned} |v_1\rangle &= \cos\theta|\mathrm{r}, \mathrm{r}\rangle + \sin\theta\tfrac{|\mathrm{r}',\mathrm{r}''\rangle+|\mathrm{r}'',\mathrm{r}'\rangle}{\sqrt{2}} &&, E_1 = \tfrac{\Delta}{2} + \sqrt{\left(\tfrac{\Delta}{2}\right)^2 + V(R)^2} \\ |v_2\rangle &= -\sin\theta|\mathrm{r}, \mathrm{r}\rangle + \cos\theta\tfrac{|\mathrm{r}',\mathrm{r}''\rangle+|\mathrm{r}'',\mathrm{r}'\rangle}{\sqrt{2}} &&, E_2 = \tfrac{\Delta}{2} - \sqrt{\left(\tfrac{\Delta}{2}\right)^2 + V(R)^2} \\ |v_3\rangle &= \tfrac{1}{\sqrt{2}}\left(|\mathrm{r}', \mathrm{r}''\rangle - |\mathrm{r}'', \mathrm{r}'\rangle\right) &&, E_3 = \Delta. \end{aligned} \tag{2.16}$$

Starting from the symmetric ground state $|\mathrm{g}, \mathrm{g}\rangle$, the system cannot be excited to the state $|v_3\rangle$ due to the difference in parity when the two atoms are exchanged. Thus only $|v_1\rangle$ and $|v_2\rangle$ have to be considered. These two new eigenstates have displaced energies due to the dipole-dipole interaction.

When being driven by a monochromatic light source, a photon will first be absorbed to

excite the system to either $|\mathrm{g,r}\rangle$ or $|\mathrm{r,g}\rangle$. The presence of a Rydberg excitation $|\mathrm{r}\rangle$ in the system then shifts the states $|v_1\rangle, |v_2\rangle$ out of resonance with the subsequent photons as depicted in Fig. 2.9. The system is thus prohibited from being doubly excited to the Rydberg level, provided that the interatomic separation is sufficiently small that the energy shift is greater than the coupling from the ground state $|\mathrm{g}\rangle$ to the Rydberg state $|\mathrm{r}\rangle$. This phenomenon is termed the "Rydberg blockade" and the interatomic distance below which the blockade happens is called the "blockade radius". In the situation where there are more than two atoms, a single Rydberg excitation in the ensemble prevents the atoms within a Rydberg-blockade radius to be excited to the Rydberg state, resulting in a Rydberg-blockade sphere.

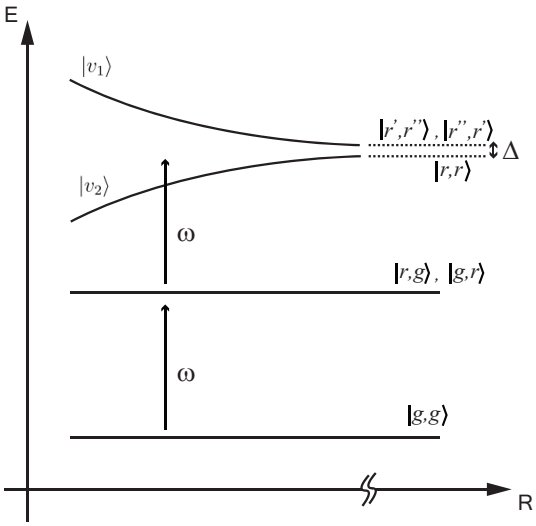

Figure 2.9: Dipole blockade prohibits the system from being doubly excited to the Rydberg level. The diagram is drawn for $\Delta > 0$.

2.3.2 Cavity QED with Rydberg Atoms

For a cold atomic ensemble of size smaller than the blockade radius, the ensemble can only accept one Rydberg excitation by virtue of the blockade effect. The atomic ensemble thus behaves like a single atom coupled to the cavity mode. We therefore expect a re-emergence of the non-linearity, much the same as the single atom-cavity scenario, with the advantage that the cavity-atom coupling strength is collectively enhanced by a factor of $\sqrt{N}$, which is the key advantage that motivates our studies.

We focus specifically on Rubidium-87 atoms. A scheme which employs a two-photon process is chosen to couple the ground state and the Rydberg state. A 780 nm NIR laser is first used to excite the atoms from the ground state $|\mathrm{G}\rangle$ to the $5P_{3/2}$ intermediate level $|\mathrm{I}\rangle$ where they are then excited to the $50S_{1/2}$ Rydberg state $|\mathrm{E}\rangle$ with a 480 nm blue laser. This realizes a three-level medium in the ladder scheme, with the 480 nm laser as the control beam, and the 780 nm laser as the probe beam.

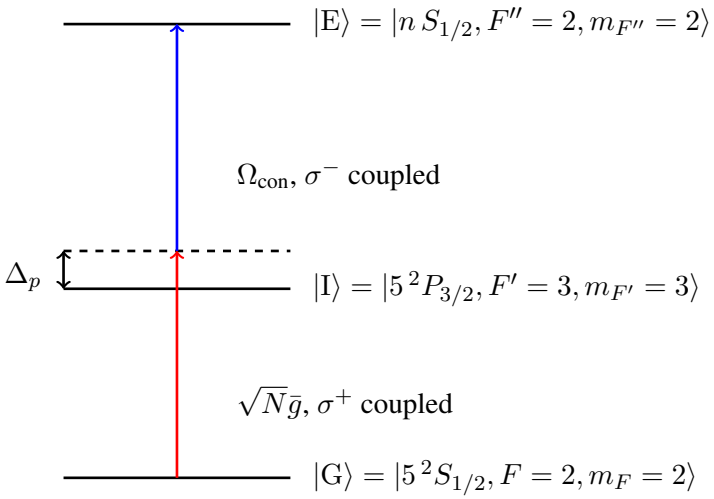

Figure 2.10: Two-photon process coupling the ground state to a Rydberg level with the 780 nm beam detuned from the intermediate state by Δ_p.

For large detuning from the intermediate state, $\Delta_p \gg \Gamma_{31}$,we can adiabatically eliminate the intermediate state and derive an effective two-level interaction Hamiltonian [15]

$$\tilde{H}_{\mathrm{eff}} = \hbar\sqrt{N}\frac{\bar{g}\,\bar{\Omega}_{\mathrm{con}}}{2\Delta_p}\hat{a}\hat{S}^\dagger + \mathrm{H.c.}, \tag{2.17}$$

where the two-photon coupling between the transition $|\mathrm{G}\rangle \leftrightarrow |\mathrm{E}\rangle$ and the cavity mode per atom is $g_{\mathrm{eff}} = \frac{\bar{g}\bar{\Omega}_{\mathrm{con}}}{2\Delta_p}$ and $\hat{S}^\dagger$ the raising operator between the two levels $|\mathrm{G}\rangle$ and $|\mathrm{E}\rangle$ defined in an analogous manner as Eq. (2.2). The effective collective coupling to the cavity mode is thus $\sqrt{N}g_{\mathrm{eff}}$. This two-level interaction can be seen as a secondary interaction on top of the vacuum Rabi splitting. The cavity-atoms system first experiences a resonant frequency shift due to the coupling between the $|\mathrm{G}\rangle \leftrightarrow |\mathrm{I}\rangle$ transition and the cavity field. Next, the detuned cavity field together with the control beam forms a Raman coupling between states $|\mathrm{G}\rangle$ and $|\mathrm{E}\rangle$, causing a secondary shift and splitting

in the system's resonant frequency. For a weak probe beam, the cavity transmission can be estimated using Eq. (2.14) as shown in Fig. 2.11.

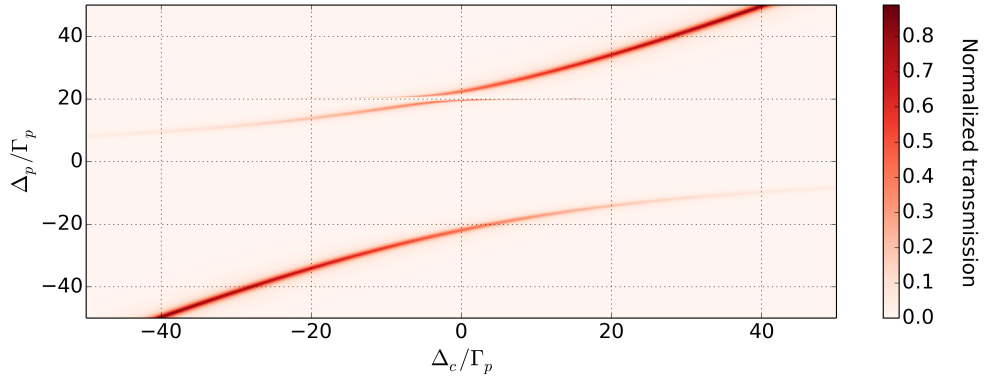

Figure 2.11: Normalized cavity transmission for a three-level intracavity medium calculated using Eq. (2.14), where $\Delta_p = \omega_p - \omega_0$ is the probe detuning, $\Delta_c = \omega_c - \omega_0$ the cavity detuning. Plotted for $\Gamma_p = 2\pi \times 6\,\text{MHz}$, $\delta_{\text{con}} = 20\Gamma_p$, $\Omega_{\text{con}} = 3\Gamma_p$, $N = 2 \times 10^5$, parameters that are typical in our setup. An extra splitting can be seen where $\Delta_p = \delta_{\text{con}}$, in accordance with the effective two-level interaction Hamiltonian Eq. (2.17)

So far, the Hamiltonian (Eq. (2.17)) has not included the dipole-dipole interactions between the Rydberg atoms. While a detailed derivation of the effective Hamiltonian including the Rydberg-Rydberg interaction can be found in [15], here we simply introduce the basic physics and discuss their resulting model. Consider an atomic sample whose extent is greater than the Rydberg-blockade radius, the whole sample will not be completely blockaded by a single Rydberg blockade sphere. Instead, $\mathcal{N}_b$ blockade spheres will be required to blockade the whole sample, making the system an $\mathcal{N}_b$ atoms system, with $1 < \mathcal{N}_b \ll N$. Assuming uniform density, we can define the atom number per blockade sphere as $n_b = N/\mathcal{N}_b$. Since the ensemble can only absorb a total of $\mathcal{N}_b$ excitations, it can be described as a collection of $\mathcal{N}_b$ spin-$\frac{1}{2}$, each coupled to the cavity mode with a coupling strength of $\sqrt{n_b} g_{\text{eff}}$. Formally, this effective interaction Hamiltonian including the dipole-dipole interactions can be written as [15]

$$\tilde{H}_{\text{eff}} = \hbar\sqrt{N} g_{\text{eff}} \left(\hat{a}\hat{S}^\dagger + \hat{a}^\dagger \hat{S}\right) = \hbar\sqrt{n_b} g_{\text{eff}} \sum_{i=1}^{\mathcal{N}_b} \left(\hat{a}\hat{S}_i^\dagger + \hat{a}^\dagger \hat{S}_i\right) \tag{2.18}$$

where $\hat{S}_i^\dagger$ ($\hat{S}$)is now the collective raising (lowering) operator restricted to the i-th blockade sphere.

In the extreme limit where the entire ensemble is blocked by one Rydberg excitation, that is $\mathcal{N}_b \approx 1$ and $n_b \approx N$, the Hamiltonian describes a Rabi model whereby one 'super-atom' is coupled to a cavity mode with coupling $\sqrt{N}g_{\text{eff}}$. This is the essential idea of the original Rydberg-cavity QED proposal [15]. In cavity QED experiments, the figure of merit is usually characterized by the single atom-cavity cooperativity, $C = \frac{g^2}{\kappa\Gamma}$. For the Rydberg-cavity QED model, one can consider an analogous cooperativity per Rydberg bubble, $\tilde{C} = \frac{n_b g_{\text{eff}}^2}{\kappa\Gamma}$. For realistically achievable experiments parameters, it should be possible to get into the strong coupling regime where $\tilde{C} \gg 1$.

The linearity of the system depends on the number of excitation n in the steady state. At very weak probe power, $n \ll \mathcal{N}_b$, we expect a transmission predicted by the linear model as in Fig. 2.11. With increasing probe power, as n approaches $\mathcal{N}_b$, more atoms are shifted out of Raman resonance with the 480 nm laser and the susceptibility of the medium reduces back to that of a two-level medium. This therefore defines a saturation intensity. In the regime of strong coupling where $\tilde{C} \gg 1$ and for a small dense ensemble for which $\mathcal{N}_b \approx 1$, the saturation intensity can be less than single photon in the cavity. In this regime, the system can only accommodate one resonant photon at a time and sub-Poissonian statistics have been predicted for the photons transmitted through the cavity [17].

3 Experimental Setup

In this chapter, we discuss the detailed setup of our experiment. The experiment is performed in an 8" Spherical Octagon vacuum chamber (Kimball Physics), pumped to a pressure of 2×10^{-10} Torr. A schematic drawing of our experiment chamber is shown in Fig. 3.1. In Sec. 3.1 we discuss the methods by which we prepare our atomic sample; in Sec. 3.2 we discuss the design of our optical cavity; in Sec. 3.3, we detail the essential lasers for the QED experiment, namely the cavity probe beam and the control beam. Finally, in Sec. 3.4, we discuss our cavity probing scheme and the general procedure of our experiment.

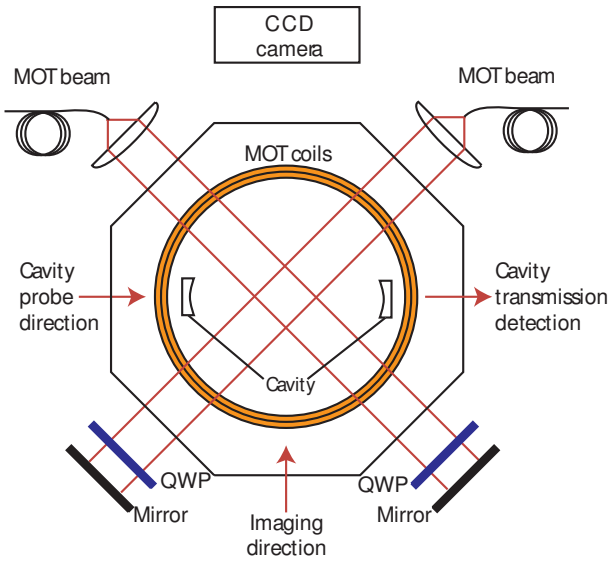

Figure 3.1: Schematic drawing of the experiment chamber. The third axis of the MOT is perpendicular to the drawing plane, hence not visible in the drawing. The three MOT beams can be seen crossing each other in the middle of the optical cavity. MOT: Magneto-Optical Trap, QWP: Quarter Waveplate

3.1 Preparation of Cold Atomic Sample

To prepare a cold atomic sample within the cavity mode, we start with a Magneto-Optical Trap (MOT). The MOT (Sec. 3.1.1) is capable of capturing the atoms directly from the hot Rubidium vapour ejected from the Rubidium dispenser. This cloud of atoms are then further cooled by a sub-Doppler cooling cycle (Sec. 3.1.2) before being loaded into the optical dipole trap (Sec. 3.1.3) formed by a cavity standing wave.

3.1.1 Magneto-Optical Trap (MOT)

A MOT combines the use of magnetic field and lasers to cool and provide 3D confinement for the atoms. A pair of current coils connected in the anti-Helmholtz configuration creates a magnetic quadrupole field. Three pairs of circularly polarized counter-propagating lasers are sent towards the trap centre along the coils' axis and two other orthogonal directions in the perpendicular plane. The lasers are red-detuned from the cooling transition so that the atoms tend to scatter more from the lasers that oppose their movement due to the Doppler effect. This creates a friction force, and hence deceleration for the atoms.

At the trap centre, the magnetic field is always zero. Around the centre, along the axis of the coils and the radial direction, the magnetic field strength varies linearly. The Zeeman sublevels of the atoms thus vary linearly along the three directions. Together with the use of red-detuned and circularly-polarized lasers, this creates a spatial imbalance in the radiation force directed towards the centre, thus achieving a 3D confinement. More details on MOT can be found in [26].

Our MOT is formed by three retro-reflected 780 nm laser detuned by -18 MHz from the $F = 2 \rightarrow F' = 3$ transition, together with a field gradient of 5 G/cm along the coils' axis. The MOT beams are derived from a Tapered-Amplifier (TA, Eagleyard Photonics EYP-TPA-0780-01000-3006-CMT03-0000) seeded by a homebuilt 780 nm

extended cavity diode laser (ECDL). The seed laser, named 'Master 1', is first phase-locked to another laser 'Master 2', which itself is locked to a Rubidium-87 transition, before seeding the TA. The phase-lock setup is shown in Fig. 3.2a. When both the lasers are locked, the frequency difference between the two lasers is equal to the frequency of the Voltage Controlled Oscillator (VCO),

$$|f_{\text{Master 1}} - f_{\text{Master 2}}| = f_{\text{VCO}}.$$

The frequency of Master 1 can therefore be tuned by changing the frequency of the VCO. With this configuration, we are able to tune Master 1 continuously from the $F = 2 \rightarrow F' = 3$ transition to the $F = 2 \rightarrow F' = 2$ transition, allowing us to use the same laser for laser cooling, optical pumping and resonant imaging.

With 10 mW of seed power, we saturate the gain of the TA, providing more than 400 mW of power at 1.7 A of current. The beam passes through an Acousto-Optical Modulator (AOM), which serves as a switch to toggle the MOT beams on and off, before going to the experiment. Taking into account the loss due to the AOM and the fibre coupling, we have 20 mW for each MOT beam. The beams are expanded to a diameter of 25.4 mm before entering the vacuum chamber (Fig. 3.1).

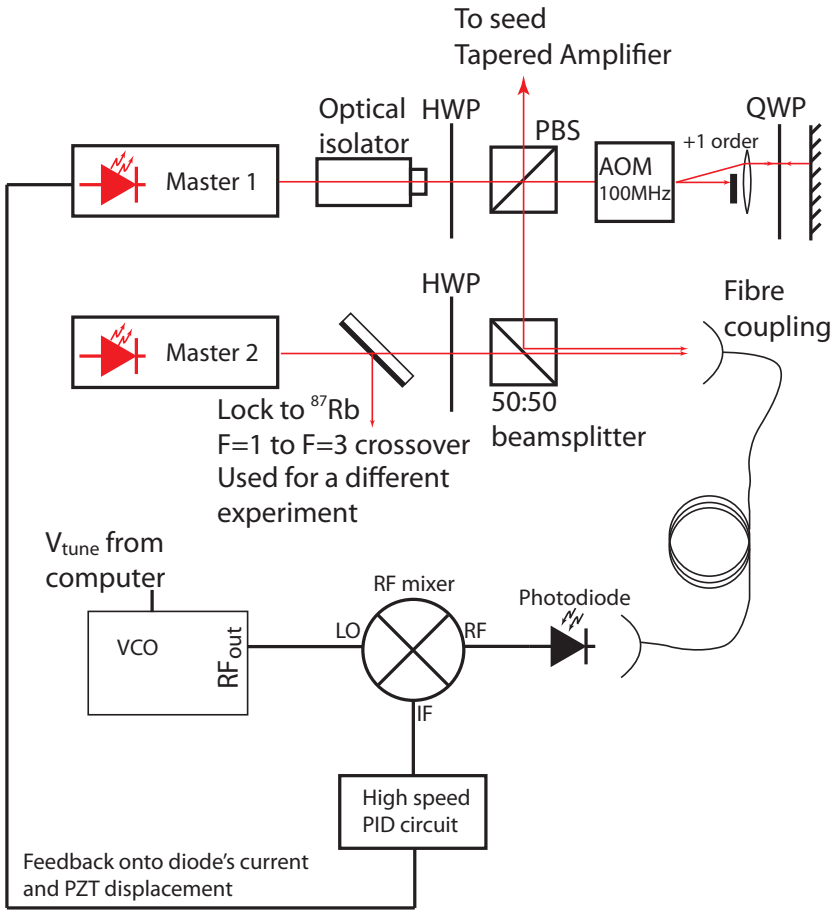

(a) Phase-lock scheme. HWP: Half Waveplate, QWP: Quarter Waveplate, AOM: Acouto-Optical Modulator, VCO: Voltage Controlled Oscillator

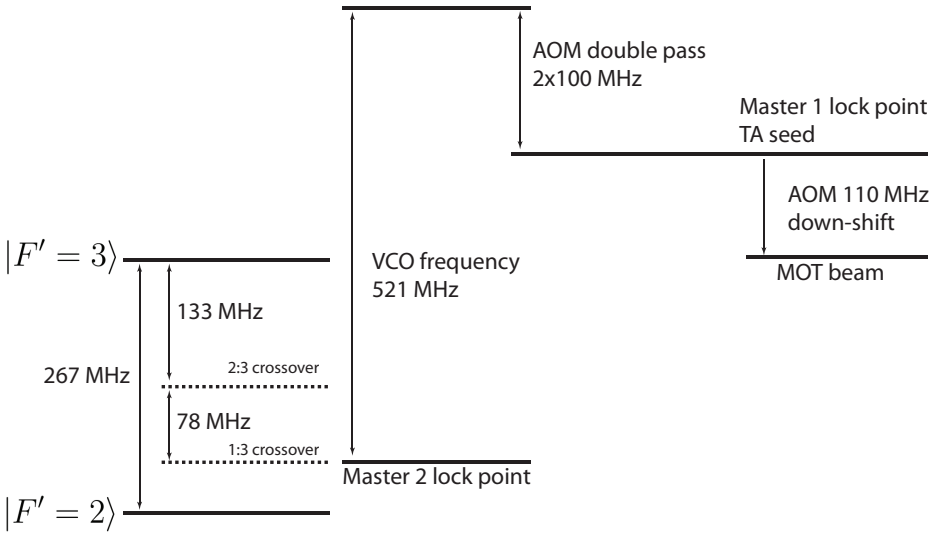

(b) Frequency settings of Master 1 and Master 2. This diagram is drawn for $f_{\mathrm{VCO}} = 521\,\mathrm{MHz}$, and the MOT beam is resonant with the $F = 2 \rightarrow F' = 3$ transition of Rb-87. By changing the VCO frequency, the MOT beam can be shifted to anywhere between the $F = 2 \rightarrow F' = 3$ resonance and the $F = 2 \rightarrow F' = 2$ resonance.

Figure 3.2: Schematic drawing of the phase-lock setup and the various frequency settings.

Due to off-resonance scattering to the $F' = 2$ state, the atoms can fall into the $F = 1$ ground state during cooling, which is 6.8 GHz detuned from the MOT beams. In order for these atoms to continue interacting with the MOT beams, another repumping laser is then used to excite these atoms to the $F' = 2$ excited state, where they can then fall back to the $F = 2$ ground state and resume the cooling cycle.

For imaging the atomic cloud, a CCD camera is installed at the top of the chamber (Fig. 3.1). We can toggle between two imaging modes: fluorescence imaging or absorption imaging. These two imaging modes are introduced in the next subsections. From fluorescence imaging measurement, we estimate that our MOT is made up of 50-60 million atoms. The temperature of the MOT, called the Doppler cooling limit, is on the order of the linewidth of the cooling transition [26],

$$T \sim \frac{\hbar\Gamma}{k_B} = 300\,\mu\text{K}.$$

Fluorescence Imaging

In fluorescence imaging, we capture the light scattered by the atoms, from which we infer the atom number. Fluorescence imaging is performed with laser intensity much higher than the saturation intensity of the atomic transition, in which case the excited state population is approximately $\frac{1}{2}$. In our experiment, the MOT beams lend themselves readily to the fluorescence imaging as the atoms in the MOT scatter light continuously. The rate at which photons are emitted is $\frac{1}{2}N\Gamma$ where N is the atom number and Γ is the transition linewidth. Taking into account the finite solid angle Ω of the imaging system (Fig. 3.3), the quantum efficiency η of the CCD camera and the exposure time τ, the total number of counts is $\frac{\Omega}{8\pi}N\Gamma\eta\tau$.

The fluorescence imaging gives a convenient way to estimate the number of atoms in the MOT, however it is also more susceptible to background noise. An iris is added to the confocal imaging system (Fig. 3.3) to single out the region of interest. The lenses are chosen to magnify the image, to the detriment of the depth of focus.

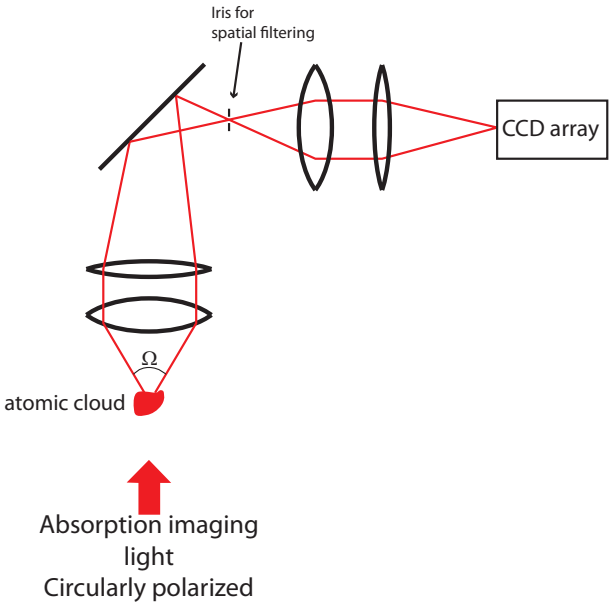

Figure 3.3: Confocal imaging system.

Absorption Imaging

In absorption imaging, we compare the intensity of a weak resonant laser beam traversing an atomic cloud to the beam intensity in the absence of the cloud. From this we deduce the amount of light scattered by the atoms, hence the column density of the atoms. Our imaging beam shares the same source as the MOT beams.

With I denoting the intensity of the beam, z the propagation distance of the beam and $\rho(x, y, z)$ the density of the atomic sample, we have

$$\frac{dI}{dz} = -\rho(x, y, z)\sigma I$$

where σ is the scattering cross section of the atoms. In general $\sigma \equiv \sigma(I)$, but in the case where I is well below the saturation intensity, $\sigma \approx \sigma_0$ is constant. This leads to

$$\frac{I}{I_0} = \exp\left(-\sigma_0 \int \rho(x, y, z)dz\right)$$

where I_0 is the laser's intensity in the absence of the atoms. The inferred column density can then be integrated to give the total atom number. Therefore, the attenuation of

the imaging beam is proportional to the atom number. In fact, σ also depends on the polarization state of the atomic cloud and the imaging beam. σ is maximized when the ensemble is perfectly polarized, for example if the ensemble is optically pumped to the highest m_F Zeeman ground state, and when the imaging beam drives only the cycling transition. For any other situations, the scattering cross section is smaller, less light is scattered, resulting in an underestimated atom number. Therefore the absorption imaging provides a convenient way to characterize the efficiency of the optical pumping in a later part of the experiment.

In practice, three images are taken in an absorption imaging setup. The first image shows the shadow of the atoms, the second image shows the initial intensity of the imaging beam I_0, the last image is taken without the imaging beam and it serves to compensate for the background noise.

3.1.2 Sub-Doppler Cooling

By detuning the laser further from the atomic transition and lowering the cooling lasers' power, a temperature much lower than the Doppler limit is achievable as a result of polarization gradient cooling [27, 28]. This cooling technique is fundamentally limited by the photon recoil energy. However, in practice, only 10-20 times the recoil temperature is achievable.

In our setup, we optimize the sub-Doppler cooling parameters to maximize the atom number in the dipole trap. The MOT number reaches a steady state after five seconds of loading, the frequency of the VCO in the phase-lock is then linearly ramped from 512 MHz to 462 MHz, increasing the MOT beam detuning from -18 MHz to -150 MHz. At the same time, the power in the MOT beams is halved. We expect the final temperature of the sample to be $\sim$ 20 μK. In the end of the cooling cycle, the repump beam is turned off 2 ms before the MOT beams so that the atoms can scatter into the $F = 1$ hyperfine manifold. This is to prevent atom loss due to hyperfine state-changing collisions.

3.1.3 Cavity-Assisted Optical Dipole Trap

For a laser beam far-detuned from the atomic transition (with respect to the atomic linewidth), the atoms' absorption of the light is negligible, however an electric dipole is induced. The interaction between the induced dipole and the optical field gives rise to a gradient force. For a laser red-detuned from the atomic transition, the gradient force points towards the intensity local maxima of the laser. An optical dipole trap exploits this gradient force exerted on the atoms to provide spatial confinement while minimizing the heating due to scattering [29].

In our experiment, the atomic cloud is loaded into an optical dipole trap at the end of the cooling cycle. The dipole trap is formed by the standing wave of an 808 nm laser coupled to the experiment optical cavity. With the Pound-Drever-Hall (PDH) method [30], the 808 nm laser is first locked to another stable reference cavity to achieve a narrow laser linewidth, while the experiment cavity is then locked to this 808 nm laser to maintain resonance. With the cavity locked to the laser, the intracavity optical power is amplified by roughly the finesse of the cavity. Therefore, the laser power required for a deep dipole trap is greatly reduced with the use of a cavity. Moreover, the atoms are trapped within the cavity mode and interact readily with the cavity, avoiding the complication of aligning the dipole trap to the cavity mode.

With 8 mW of laser power coupled to the fundamental Hermite-Gaussian mode of the cavity, the intracavity circulating power is ~ 2.6 W, taking into account the mirrors' absorptive and scattering losses. With this, we achieve a 570 μK-deep trap, corresponding to 12 MHz AC-Stark shift for the $5S_{1/2}$ ground state. The density in the dipole trap is very high ($\sim 10^{13}\,\mathrm{cm}^{-3}$), imaging the atoms in the dipole trap tends to undercount the atom number due to the limited dynamic range of the CCD camera. The dipole trap is thus turned off 0.2-1 ms before the absorption imaging so that the density decreases as the cloud undergoes ballistic expansion. The measured lifetime of the trap is 250 ms. We note that this is substantially less than a lifetime of two seconds previously observed in an 808 nm cavity assisted dipole trap [18]. This is attributed to the heating and loss

due to the residual fluctuation in the intracavity intensity even after active stabilization.

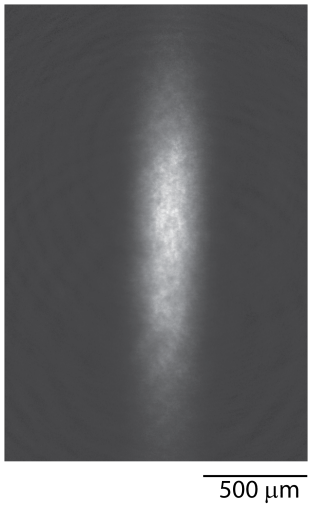

(a) Image of the dipole trap.

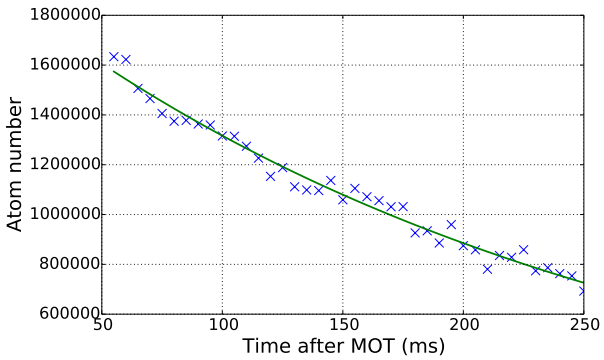

(b) Plot of atom number against the dipole trap hold time. The fit gives a trap lifetime of 252 ± 6 ms.

Figure 3.4: Measurement of the dipole trap lifetime.

3.1.4 Optical Pumping

Optical pumping is an important technique in preparing our atomic ensemble in the desired state. In our experiment, we pump the ensemble using the same beam as the imaging beam together with a magnetic field pointing along the propagation axis of the pumping beam. This beam is tuned into resonance with the $5S_{1/2}, F = 2 \rightarrow 5P_{3/2}, F' = 2$ transition and is circularly-polarized such that one of the Zeeman sub-states with the maximum $|m_F|$ is a dark state.

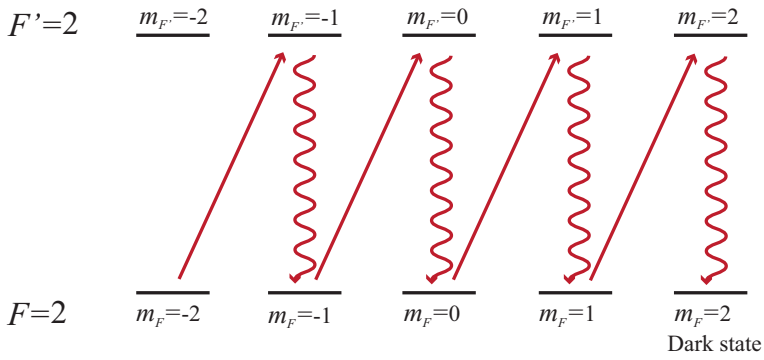

Figure 3.5: Optical pumping using the $5S_{1/2}, F = 2 \rightarrow 5P_{3/2}, F' = 2$ transition. In this diagram, it is assumed that we are pumping towards the $|m_F = 2\rangle$ state.

Once the atoms fall into the dark state, collisions between the atoms do not lead to the change in m_F states as it is impossible to redistribute the angular momentum quantum number. They thus remain in the dark state even long after the optical pumping pulse. If the magnetic field is then adiabatically modified (as compared to atom's Larmor frequency), the polarization of the atoms will follow the direction of the magnetic field. Special care needs to be taken to ensure that the magnetic field never crosses zero during the process. This is because the Larmor frequency vanishes at the zero point and the adiabaticity can be broken.

3.2 Optical Cavity

The optical cavity serves to amplify the coupling between the atoms and the electromagnetic field. For this, the cavity mirrors need to have high reflectivity and low loss to enhance the lifetime of photons in the cavity. Our optical cavity is constructed with two concave mirrors with a broadband high reflectivity coating provided by ATFilms. The mirrors' coating is specified to have transmissive loss of $\mathcal{T} \approx 0.25\%$ and absorptive loss $\mathcal{A} < 4$ ppm for wavelengths ranging from 650 nm to 1 μm. The reflectivity of the mirrors' coating depends slightly on the wavelength, therefore the finesse of the cavity varies with wavelength.

The specifications of our optical cavity at the relevant wavelengths are summarized in the Table 3.1.

Description	Value	Unit
Length	6.3	cm
Radius of curvature of cavity mirrors	10	cm
Diameter of cavity mirrors	1.27	cm
Waist at 780 nm	107	μm
Waist at 808 nm	109	μm
Finesse at 780 nm	900	
Finesse at 808 nm	1300	
Finesse at 480 nm	3	

Table 3.1: Specifications of our optical cavity.

The cavity QED parameters are

κ	$2\pi\times2.65$	MHz
g_0	$2\pi\times0.195$	MHz
Γ_{31}	$2\pi\times6$	MHz
Γ_{23}	$2\pi\times3.2$	kHz

Table 3.2: Cavity QED parameters. g_0 is the maximum coupling strength between the atoms and the cavity.

Our cavity is long and of moderate finesse, this design allows us to create the cold atom cloud directly within the cavity as shown in Fig. 3.1, avoiding the complications of transporting the cold atoms. The length of the cavity is controlled by two pieces of shear-mode PZT below the cavity mirrors and is actively stabilized by locking the cavity length to a stable 808 nm laser using the PDH technique as mentioned in Sec. 3.1.3.

3.2.1 Electric Field Shielding

Because Rydberg atoms have high polarizability, they are very sensitive to stray electric field. To shield the atoms from the electric field created by the high voltages applied on the PZT's, the PZT's are surrounded by grounding shields made of aluminium.

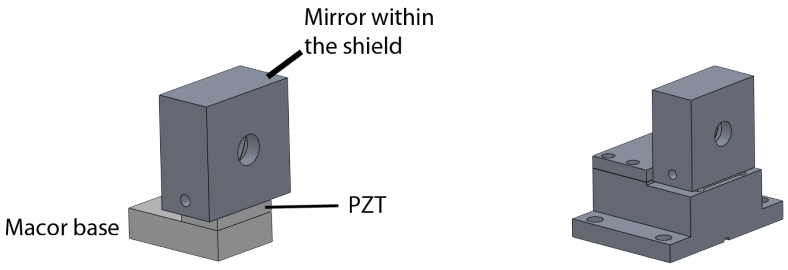

(a) Shielded mirror.

(b) Full ground shield.

High voltage is applied onto the bottom of the PZT through an electrical lead created using silver epoxy, and the top is grounded. The cavity mirrors reside in two aluminium

ground shields mounted directly onto the PZT with silver epoxy. Another advantage in doing so is that we could keep the mirrors from the line-of-sight of the Rubidium dispenser, which helps to prevent the mirrors from being coated with Rubidium. A small tapped hole on the side of the mirror shields allows it to be grounded via a gold ribbon.

3.3 Cavity QED Laser Systems

3.3.1 Cavity Probe beam

In order to resolve the narrow features in the cavity transmission due to the three-level ladder coupling scheme, the cavity needs to be driven by a laser of narrow linewidth. For this, we opted to build a ECDL with a long extended cavity to reduce the linewidth and its the sensitivity to current noise [31]. The extended cavity length is $\approx 13\,\text{cm}$, the expected linewidth is on the order of 1-10 kHz. The frequency shifting of the cavity probe beam is shown in Fig. 3.6.

The laser is first locked to the same reference cavity at about $1.1\,\text{GHz}$ above the $|F = 2\rangle \rightarrow |F' = 3\rangle$ transition. The beam is then double-passed through an AOM to down-shift the frequency by 400 MHz. Finally, an EOSpace device is used put on two frequency sidebands of $600 - 700\,\text{MHz}$, one of which is close to the $|F = 2\rangle \rightarrow |F' = 3\rangle$ transition. This sideband will be the one probing the cavity. A stripper cavity is used to filter out the unwanted sidebands at the output of the EOSpace device before the experiment cavity.

The RF signal driving the AOM is derived from a homebuilt Direct Digital Synthesizer (DDS). The DDS board can be configured to perform a continuous linear frequency sweep within a very short time interval ($<1\,\text{ms}$), allowing us to sweep the probe beam across a range of frequencies in a short time.

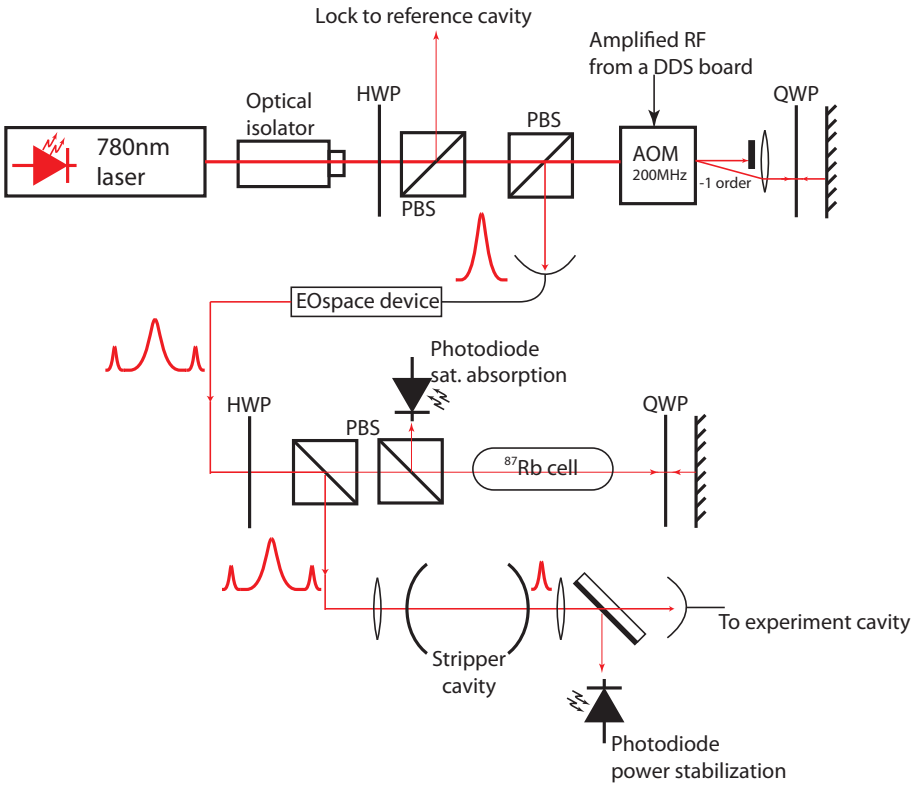

Figure 3.6: Schematic diagram of 780 nm cavity probe beam setup. DDS = Direct Digital Synthesizer.

3.3.2 480 nm Control Beam

The 480 nm control beam coupling the $5P_{3/2}$ state to the $nS_{1/2}$ Rydberg state is generated by frequency-doubling a 960 nm laser using a periodically-poled Potassium titanyl phosphate crystal (PPKTP). The 960 nm pump laser is derived from a Tapered Amplifier (TA) seeded by an ECDL. Single-pass frequency-doubling has in general very low efficiency ($\sim$ 1%/W or less), therefore a bow tie doubling cavity [32] is constructed around the PPKTP crystal in order to amplify the optical field irradiating the crystal as shown in Fig. 3.7. Frequency doubling using periodically-poled crystals is very sensitive to the temperature of the crystals as the period of the domain needs to match the wavelength in order to maintain the quasi-phase-matching condition. The temperature of our crystal is stabilized by a peltier cell.

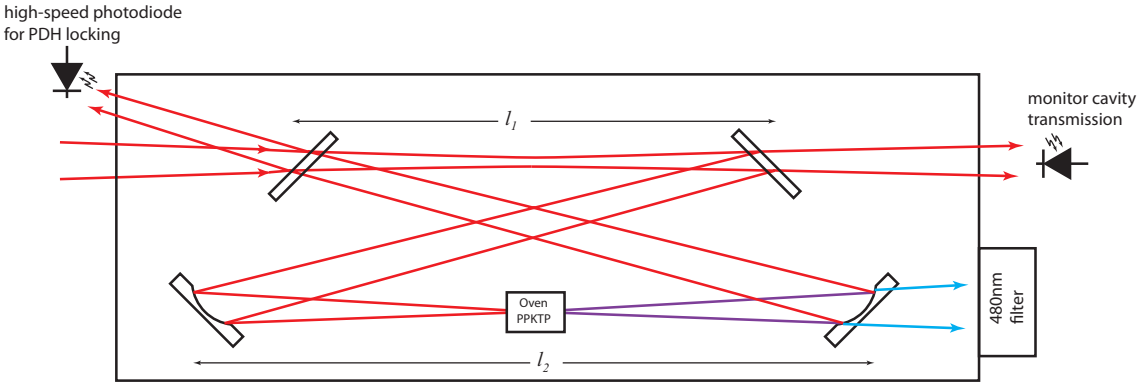

Figure 3.7: Schematic drawing of the 480 nm bow tie doubling cavity. The PPKTP is temperature stabilized in the oven by a peltier cell.

Description	Value	Unit
ℓ_1	72	mm
ℓ_2 (physical path)	113.23	mm
Radius of curvature of concave mirrors	100	mm
Length of crystal	10	mm
Folding angle	15	degree
Optical coupler's reflectivity @ 960 nm	0.99	
Horizontal waist at short arm	169	μm
Vertical waist at short arm	201	μm
Horizontal waist at crystal	65	μm
Vertical waist at crystal	67	μm

Table 3.3: Specifications of the 480 nm doubling cavity. The cavity geometry is designed to have a circular waist at the crystal, but this requires an elliptical beam in the short arm [33].

With 350 mW of 960 nm beam incident onto the doubling cavity, only $\sim 50\%$ is mode-matched to the cavity due to the rectangular mode shape at the output of the TA and ~ 100 mW of 480 nm beam is generated. We estimate an overall doubling efficiency of $\sim 57\%$.

3.4 Cavity Probing

The cavity is probed 50 ms after the MOT is turned off to ensure that the MOT cloud has dispersed and only the atoms loaded in the dipole trap remain. To measure the resonant frequency of the atoms-cavity system described by Eq. (2.1) and Eq. (2.17), we sweep

the cavity probe beam over a range of frequency and measure the cavity transmission using a Single Photon Counting Module (SPCM). As shown in Fig. 3.8, two dichroic mirrors are used to combine the probe laser with the 808 nm dipole beam and the 480 nm control beam.

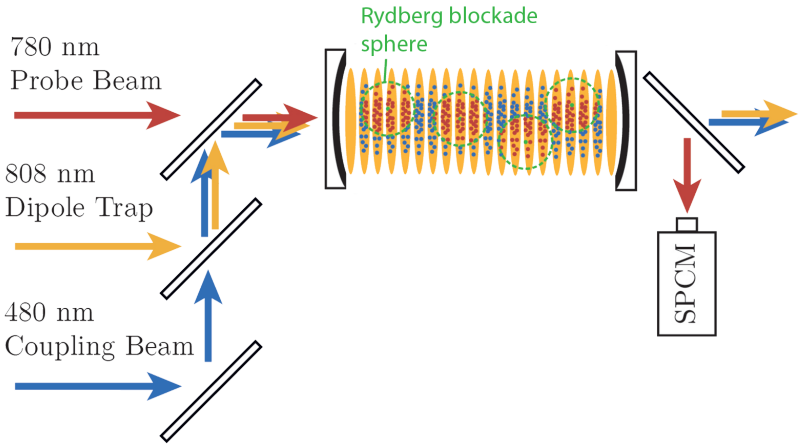

Figure 3.8: Cavity probing scheme. Dichroic mirrors are used to combine the different lasers. SPCM: Single Photon Counting Module.

Both the 780 nm and the 808 nm beams are coupled to the fundamental mode of the cavity. The 480 nm beam is sent along the cavity axis so that all the atoms are irradiated and participate in the three-level scheme. Our cavity has a very low finesse at 480 nm, it is therefore difficult to distinguish the different spatial modes.

In each run of the experiment, the frequency of the probe beam is swept up and down over a range of 50 MHz or less. The 480 nm is only turned on during one branch of the ramp as shown in Fig. 3.9. The cavity transmission for these two branches are compared to observe the effect of the 480 nm control beam. The atom loss during the two ramps can also be deduced by comparing the difference in the resonant frequencies.

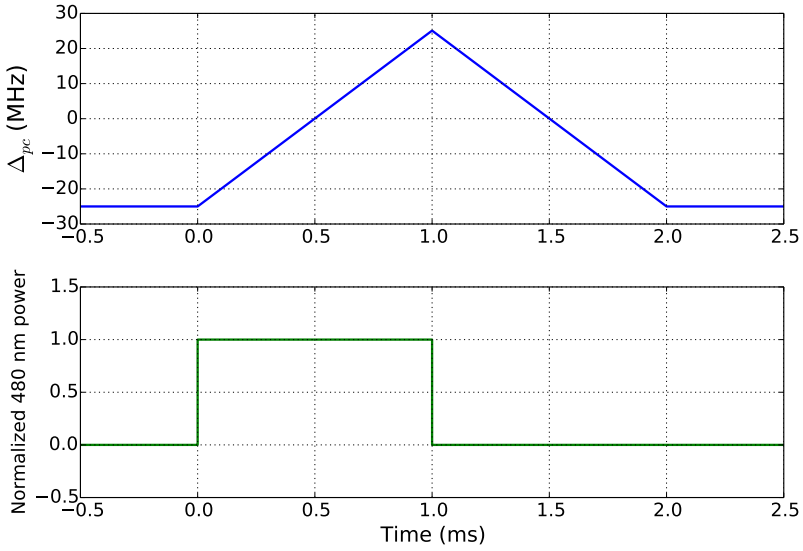

Figure 3.9: An example of frequency ramping. Δ_{pc} is the probe detuning from the cavity resonance as in Eq. (2.14). The 480 nm beam is only turned on during the first ramp.

4 Result and Discussion

In this chapter, we present some preliminary results of the project and outline the difficulties encountered. While initially we attempted to observe the effect of three-level dispersion in the cavity spectra, these attempts were unsuccessful. We believe this to because of the inhomogeneous broadening due to the variation of the AC Stark shift across the density distribution of the atomic cloud. We then present the measurements characterizing this inhomogeneous broadening and our investigation into the three level dispersion without the cavity.

4.1 Vacuum Rabi Splitting

To verify the collective coupling between the cavity and the atoms, the cavity-atoms system is first probed without the 480 nm control beam. An example of the cavity transmission measurement performed at a cavity detuning of 10 MHz is shown in Fig. 4.1.

As shown in Eq. (2.7), the resonant frequency shift scales as $\sqrt{N}$ where N is the number of atoms coupled to the cavity. In view of the limited frequency bandwidth of our AOM (40 MHz), the atom number is substantially reduced by turning down the Rubidium dispenser to collect this particular set of data. The inferred atom number is ~ 4500. The maximum shift for our system can be as much as 200 MHz with 3 million atoms.

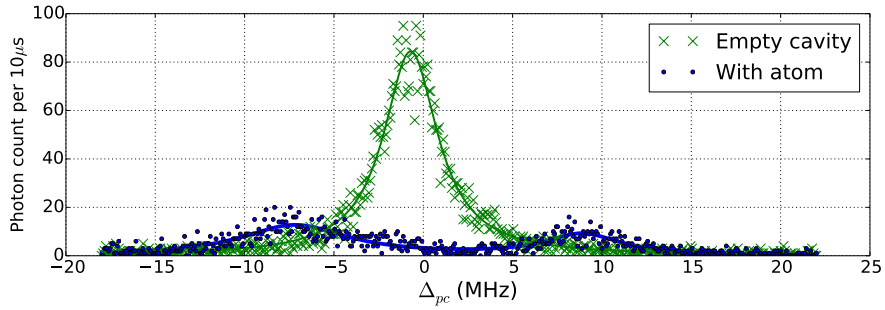

Figure 4.1: Measurement of the cavity transmission with a cavity detuning $\Delta_c = 10$ MHz. The solid lines are the respective least-square fits to the Lorentzian model.

In Fig. 4.1, the transmission peak can be seen split into two symmetrically in the presence of the atoms. This behaviour is expected if the cavity resonant frequency coincides with the atomic resonant frequency. Although the cavity is nominally 10 MHz detuned from the atomic transition, the AC Stark shift due to the 808 nm dipole beam shifts the atoms into resonance with the cavity. This observation also provides us a method to measure the AC Stark shift.

With the cavity on resonance with the atoms, each excitation of the system is shared equally by the atoms and the cavity field. Photons can therefore be lost as a consequence of atoms scattering into the free space and a decrease in cavity transmission will be observed. Fig. 4.1 shows a significant decrease in cavity transmission, the transmission is only $\sim 15\%$ in the presence of the atoms. This is consistent with the model from Eq. (2.14), as plotted in Fig. 2.7.

As an additional remark, the empty cavity transmission is not centered around zero because of the frequency drift of our reference cavity.

4.2 AC Stark Shift

As mentioned in previous section, the vacuum Rabi splitting provides a convenient way to measure the AC Stark shift due to the 808 nm dipole beam. If we sum up the two

resonant frequencies in Eq. (2.7), with the reference point ω_c

$$(E_+^{(1)} - \hbar\omega_c) + (E_-^{(1)} - \hbar\omega_c) = -\hbar\Delta_c \ ,$$

the resulting frequency is independent of the atom number and is proportional to Δ_c. Therefore, to deduce the AC Stark shift, it suffices to locate the midpoint of the two transmission peaks in the presence of the atoms while varying the cavity detuning Δ_c. This has the advantage that the measurement result is independent of the atom number which fluctuates from shot to shot.

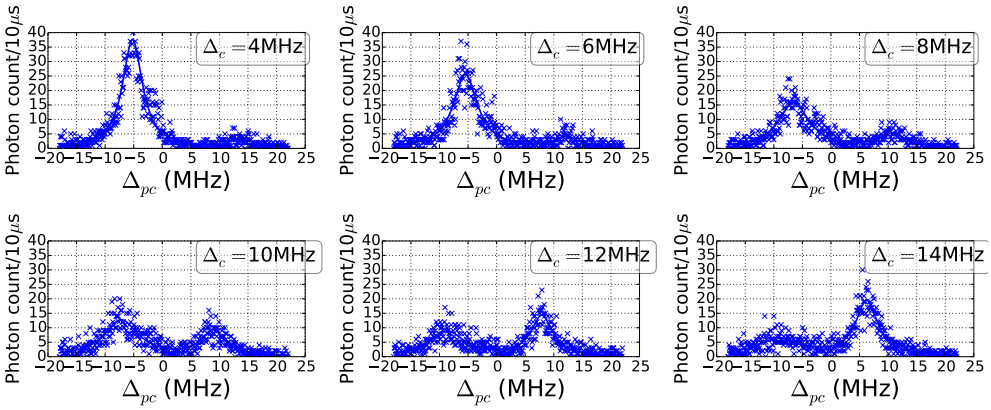

Figure 4.2: Cavity transmission for different nominal cavity detunings.

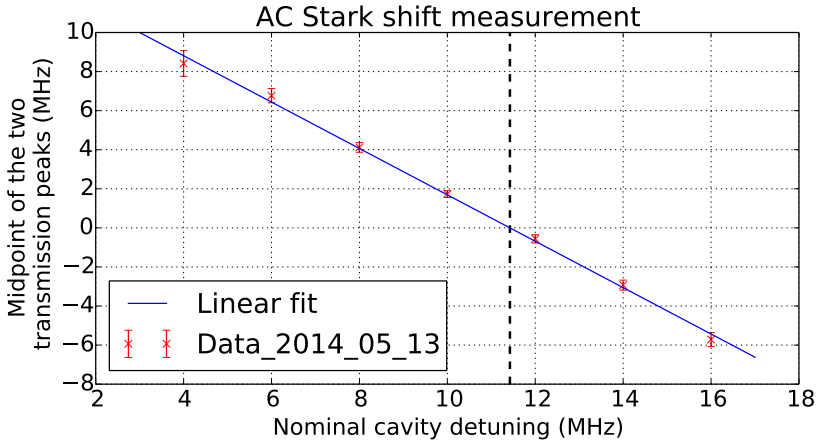

Figure 4.3: Plot of the midpoint versus the nominal cavity detuning. The dashed line marks the zero-crossing point, corresponding to a nominal cavity detuning of 11.4 MHz.

As shown in Fig. 4.3, the zero-crossing point is located at a nominal cavity detuning of 11.4 MHz. At this frequency, the cavity frequency ω_c matches that of the transition

$|\mathrm{G}\rangle \rightarrow |\mathrm{I}\rangle$. From the inferred intracavity circulating power of 808 nm dipole beam, we calculate a peak Stark shift of 16 MHz. This measurement suggests the mean AC Stark shift, 11.4 MHz, is in fact 30% below this value. This could be due to the underestimation of the cavity transmission at 808 nm or the inhomogeneous broadening explained in the next subsection.

4.2.1 Inhomogeneous Broadening

At each trap site of the intracavity lattice, the atoms localize at the bottom of the potential well with a certain spread in both the cavity axial and transverse directions due to the finite temperature of the sample. Since the trapping potential is equivalent to the AC Stark shift of the ground state, the atoms at different distances from the trap centre would then experience different detunings from the probe beam, as shown in Fig. 4.4.

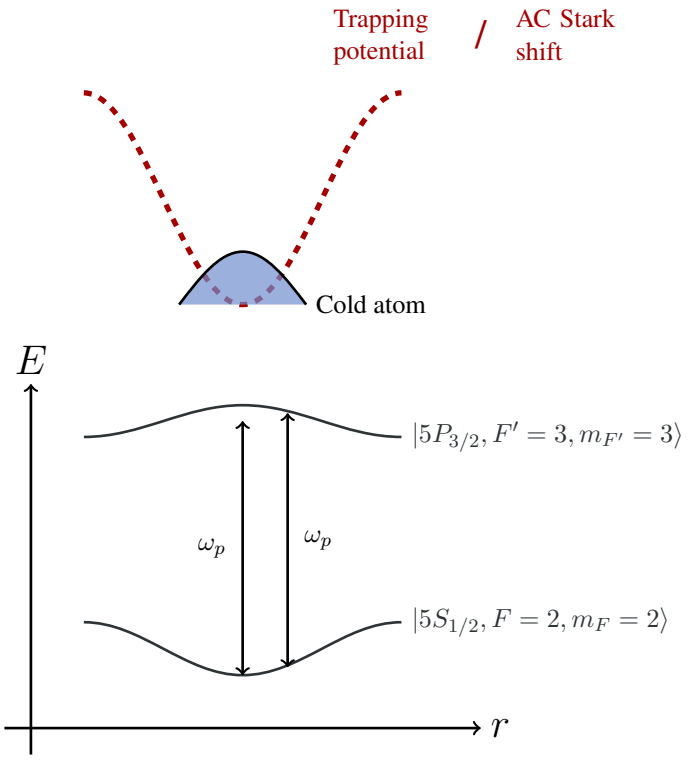

Figure 4.4: Illustration of the inhomogeneous broadening due to the dipole beam. The upper state is anti-trapped while the ground state is trapped.

As a consequence, the susceptibility of the medium has to be averaged over the spatial

distribution of the atomic sample, resulting in an effective broadening. Essentially, the resulting susceptibility is the convolution of the three-level susceptibility function χ with the Stark shift density profile of the atoms.

The measured temperature our atomic sample is $\approx 100\,\mu$K, only about one-sixth of the trap depth ($570\,\mu$K). The atoms can therefore be found significantly far from the trap centre. Fig. 4.5 shows the approximate probability density distribution of the Stark shift experienced by an atom in the trap for a trap depth to temperature ratio $\eta = 5$, calculated in the harmonic approximation of the trapping potential.

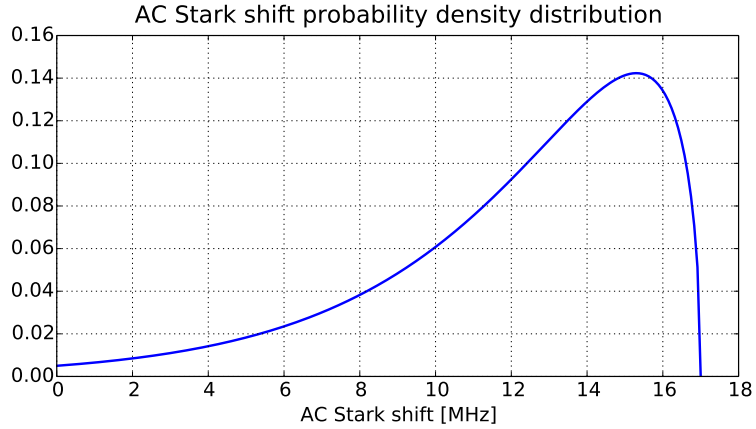

Figure 4.5: Probability density distribution of the AC Stark shift experienced by the atoms for $\eta = 5$.

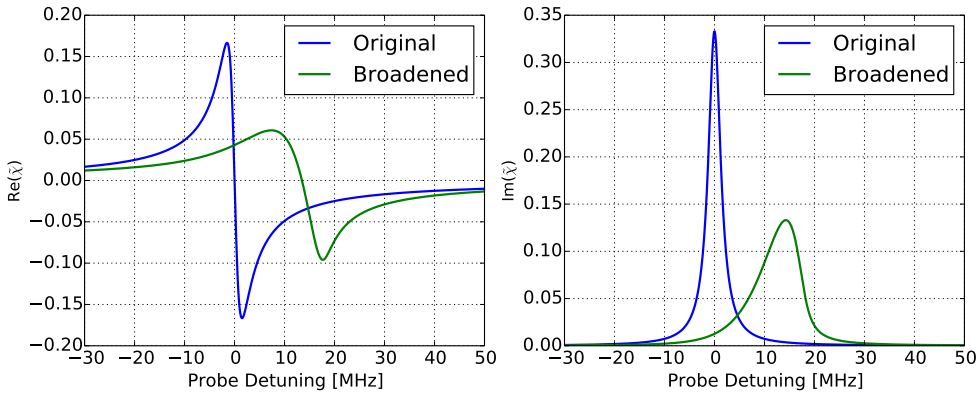

Figure 4.6: Broadened two-level susceptibility of the atomic sample.

With this taken in the account, a non-linear fit is performed on the experimental data shown in Fig. 4.2 with the maximum AC Stark shift, the atom number N and η as free parameters. The result of the fit is displayed in Fig. 4.7. This fitting shows a good

agreement with our measurement, suggesting a maximum AC Stark shift of 17 MHz with $\eta = 5$.

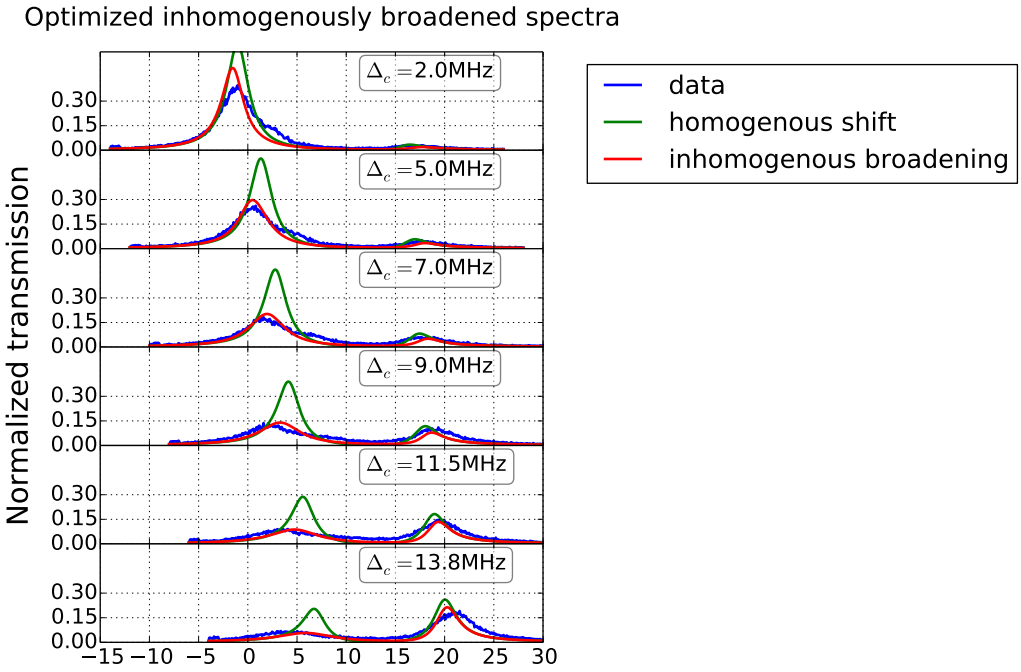

Figure 4.7: Comparison of the data to the theoretical spectra predicted with inhomogeneous broadening (red) and without (green). For the inhomogeneous broadened spectra, the model parameters are $\eta = 5$, peak Stark shift = 17 MHz, and $N = 3500$. For the homogeneous shift model, the parameters are a fixed shift of 13 MHz and $N = 3500$.

4.3 Effect of Inhomogeneous Broadening on Three-level Dispersion

Due to the inhomogeneous Stark shift, the atoms at different distances from the trap centre experience different Raman detunings from the two-photon resonance. This essentially broadens the features of the three-level dispersion through the averaging process mentioned previously. Fig. 4.8 shows the broadened susceptibility, with the broadened two-level susceptibility included for comparison.

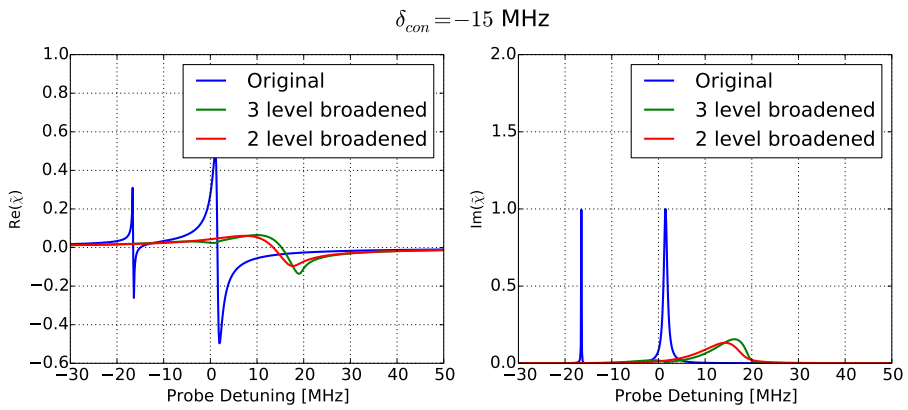

Figure 4.8: Broadened two-level and three-level susceptibility of the medium $\Omega_{\text{con}} = 10\,\text{MHz}$ and $\delta_{\text{con}} = -15\,\text{MHz}$.

We see that when the inhomogeneous broadening is wider than the two-photon coupling, the three-level susceptibility reduces to one somewhat closer to that of a two-level medium. The cavity transmission is thus the same as a two-level medium, rendering the effect of the 480 nm control beam unobservable.

4.4 Free Space EIT

During the cavity probing phase, it is preferable that the atoms stay trapped so that the coupling strength stays constant and also for the ease of the data analysis. The use of a dipole trap is hence necessary. To our knowledge, the influence of a deep optical dipole trap on the Rydberg states has not been well-studied. Therefore, we plan to perform an EIT experiment similar to the one described in Ref. [22], but with the atoms in the dipole trap, to understand the effect of having a dipole field. The experiment consists of measuring the change in absorption of a 780 nm probe beam by the atomic sample induced by the use of a control beam. This would also allow us to have a better estimate of the Raman coupling strength.

Fig. 4.9 shows an image of the atoms in the dipole trap, taken with the 480 nm blue beam shining from the side of the chamber. A dark trace can clearly be seen in the image where the 480 nm beam traverses the atomic sample. This suggests either the

presence of a transparency window due to the 480 nm control beam or atom loss due to the ionization of Rydberg atoms or other loss mechanisms.

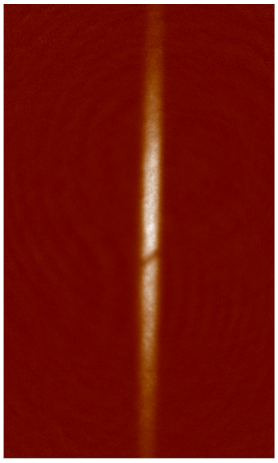

Figure 4.9: 480 nm beam from the side illuminating the atoms in the dipole trap.

This is the first indication that we successfully drive the Rydberg transition. In order to maximize the coupling from the intermediate state $|\mathrm{I}\rangle$ to the Rydberg state $|\mathrm{E}\rangle$, the atomic ensemble needs to be optically pumped and the 480 nm control beam needs to be sent along the quantization axis with the appropriate circular polarization (Fig. 2.10). The experimental setup is thus modified so that the control beam is counter-propagating with the imaging beam as shown in Fig. 4.10.

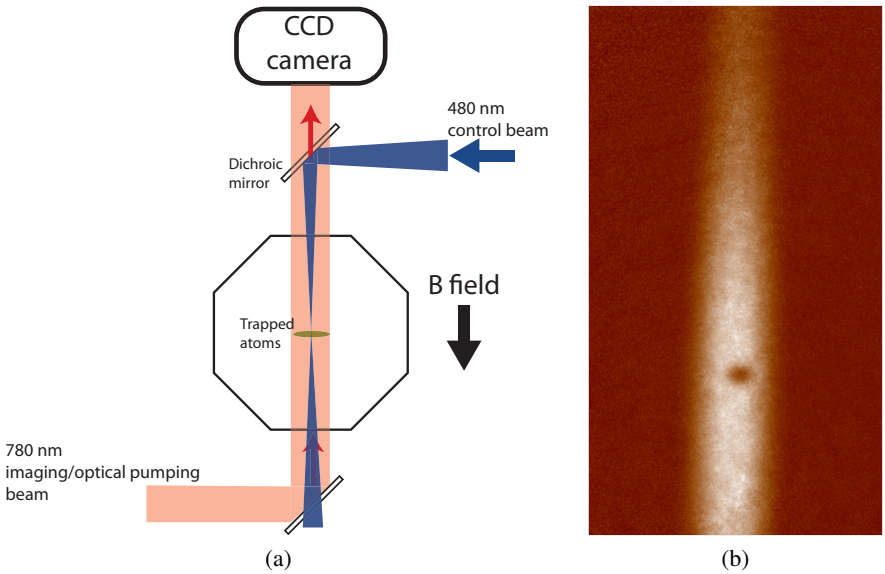

Figure 4.10: (a) Setup for the EIT experiment. (b) A typical image of the dipole trap showing a hole of lost/transparent atoms in the presence of the blue beam.

As a first implementation, the experiment is performed without the dipole trap so as not to complicate the analysis. In each run of the experiment, the dipole trap is turned off 0.2 ms before imaging. The control beam is then turned on at the same time as the imaging beam. 30 mW of control beam is focused to a waist of 20 μm onto the atoms, giving a Rabi frequency $\Omega_{\text{con}} = 2\pi \times 20$ MHz. The region irradiated by the control beam again shows a dark spot and has very low optical density. The imaging detuning is then varied from -30 MHz to 17 MHz to deduce the variation of the optical density with the probe detuning. The result is shown in Fig. 4.11.

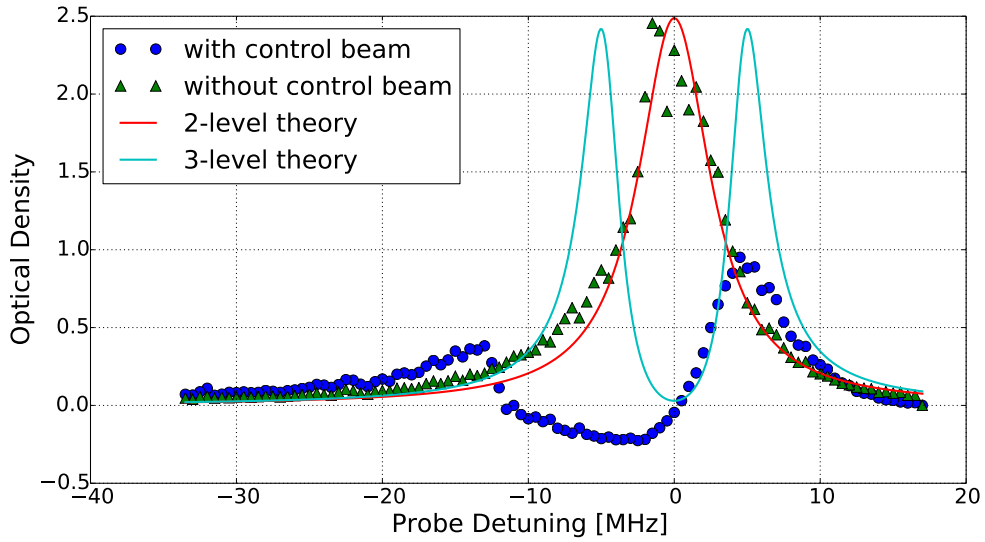

Figure 4.11: Optical density of the atomic sample with the control beam on resonance with the $|\text{I}\rangle \leftrightarrow |\text{E}\rangle$ transition.

In Fig. 4.11, we first notice that the average optical density goes below zero for certain negative detunings in the presence of the control beam. This signifies that the intensity in the first absorption image is higher than that in the second absorption image (see Sec. 3.1.1 for the implementation of absorption imaging). This is because of the lensing effect of the three-level atomic sample when a detuned imaging beam is used [34]. Because of the small waist of the control beam, when the imaging beam is detuned from the atomic transition, the light experiences a spatial dependent phase shift, as illustrated in Fig. 4.12. Assuming uniform density near the centre of the cloud, this spatial dependent phase shift translates into spatial dependent optical path length. The atomic sample hence acts as a lens that focuses the light from the surrounding onto the pixels of interest.

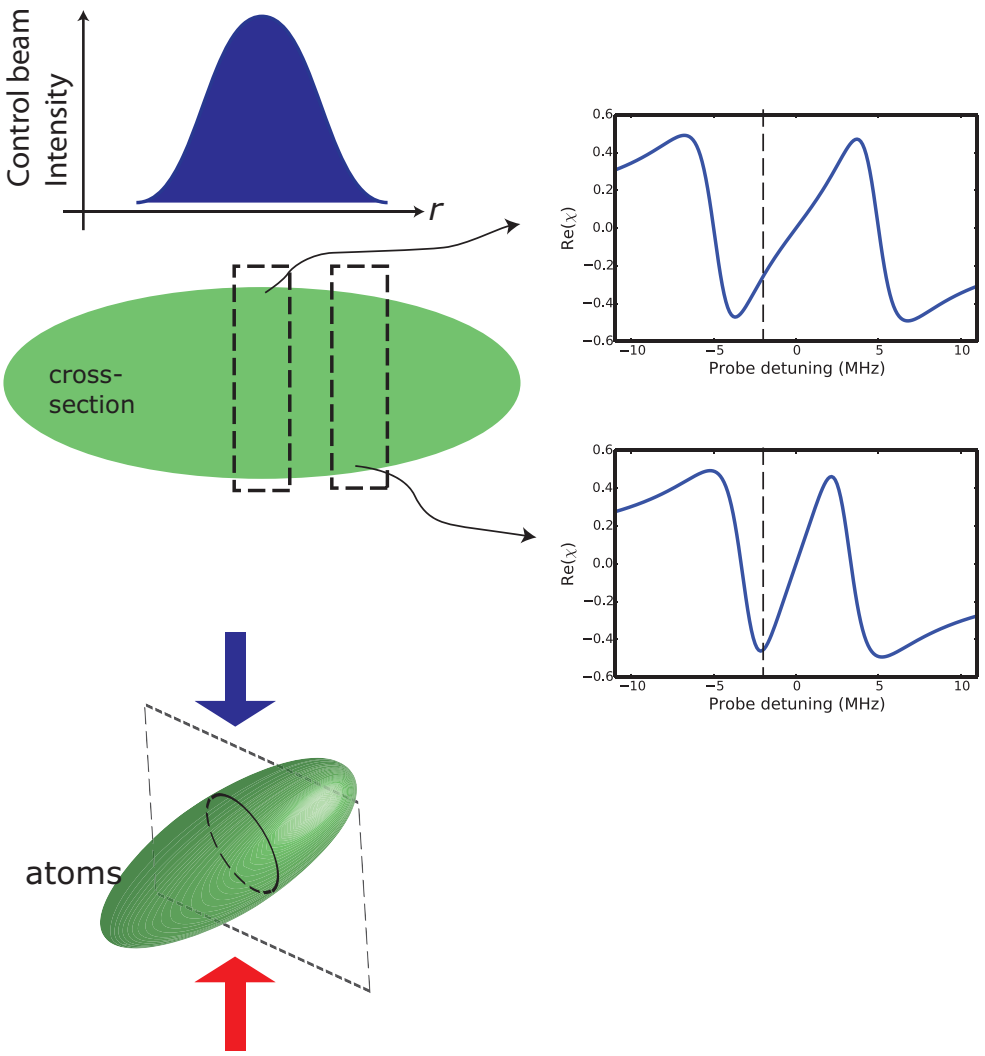

(a) Spatial dependent accumulated phase.

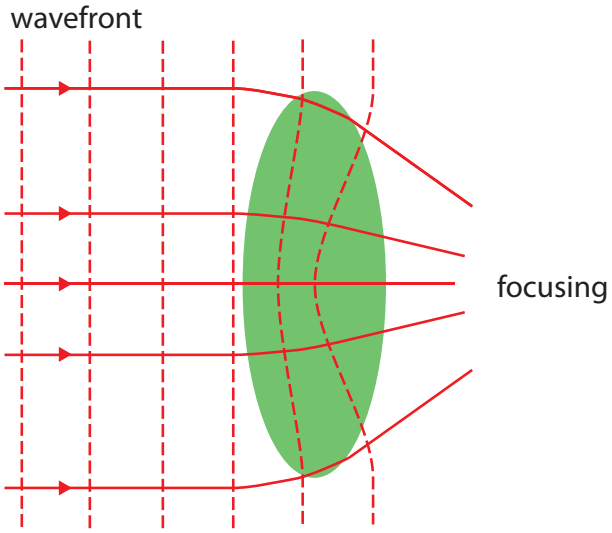

(b) Focusing of the beam due to the spatial dependent phase shift.

Figure 4.12: EIT lensing effect.

Furthermore, a dip in the optical density can also be seen when the imaging detuning is varied across the atomic resonance in the presence of the control beam, indicating a drop in absorption. The separation between the two peaks shows that the coupling $\Omega_{\text{con}} \approx 20\,\text{MHz}$ as expected. However, the spectrum thus obtained is not symmetric as it ought to be. We suspect that the lensing effect might have been the cause of this asymmetry, thus the implementation of this experiment needs to be modified so as to include also the pixels outside the zone of interest.

5 Conclusion and Outlook

In summary, an initial experimental setup has been constructed in an attempt to explore the quantum non-linearity of a cavity QED system with the use of Rydberg atoms. Systematic experiments have been carried out to study the influence of the dipole beam on the Rydberg atoms. At the current stage, we have not observed the effect of a three-level coupling on the cavity and we attribute this to the inhomogeneous broadening. In the following, we outline our future goals and discuss our approach.

The typical coupling between the cavity mode and the two-photon transition is ~ 2 MHz, the inhomogeneous broadening of about 3 MHz thus presents a very big issue as it completely washes out the three-level dispersion. To circumvent this problem, either the temperature of the atomic sample needs to be lowered substantially, or the maximum AC Stark shift needs to be reduced. Our current plan is to perform an optical evaporative cooling on the sample by ramping the trap depth to roughly one twentieth of the current value. This on the one hand reduces the AC Stark shift experienced by the atoms, on the other hand the ensemble will be colder and denser. Alternatively, we can also use another tightly focused dipole beam from the cavity transverse direction to first form a dense atomic sample before loading the atoms into the current 808 nm lattice to obtain a smaller but denser and colder sample. A smaller sample size also allows us to focus the control beam to a smaller waist to enhance the two-photon coupling.

A special emphasis needs to be given to the importance of the spatial extent and the density of atomic ensemble in achieving quantum non-linearity in a Rydberg-cavity QED system. To achieve quantum non-linearity, the number of Rydberg blockade spheres or

bubbles required to blockade the whole ensemble need to be small so that the atomic ensemble resembles a single atom, yet the atom number needs to be large in order to enhance the coupling strength. It therefore boils down to having a small and dense atomic sample. As the dipole-dipole interaction strength scales as n^{11}, the choice principle quantum number of the Rydberg state also plays an important role. At the limit of our current setup, it should be possible to push the number of blockade spheres down to ≈ 2 by reducing the sample size to $\approx 50\,\mu$m along the cavity axis and by changing our choice of Rydberg state to one with $n \approx 100$.

Bibliography

[1] Michael A Nielsen and Isaac L Chuang. *Quantum computation and quantum information*. Cambridge university press, 2010.

[2] Shu-Shen Li, Gui-Lu Long, Feng-Shan Bai, Song-Lin Feng, and Hou-Zhi Zheng. Quantum computing. *Proceedings of the National Academy of Sciences*, 98(21):11847–11848, 2001.

[3] H_J Kimble. The quantum internet. *Nature*, 453(7198):1023–1030, 2008.

[4] Edwin T Jaynes and Frederick W Cummings. Comparison of quantum and semi-classical radiation theories with application to the beam maser. *Proceedings of the IEEE*, 51(1):89–109, 1963.

[5] Kevin M Birnbaum, Andreea Boca, Russell Miller, Allen D Boozer, Tracy E Northup, and H Jeff Kimble. Photon blockade in an optical cavity with one trapped atom. *Nature*, 436(7047):87–90, 2005.

[6] L.-M. Duan and H. J. Kimble. Scalable photonic quantum computation through cavity-assisted interactions. *Phys. Rev. Lett.*, 92:127902, Mar 2004.

[7] P Maunz, T Puppe, I Schuster, N Syassen, PWH Pinkse, and G Rempe. Normal-mode spectroscopy of a single-bound-atom–cavity system. *Physical review letters*, 94(3):033002, 2005.

[8] I Schuster, A Kubanek, A Fuhrmanek, T Puppe, PWH Pinkse, K Murr, and G Rempe. Nonlinear spectroscopy of photons bound to one atom. *Nature Physics*, 4(5):382–385, 2008.

[9] Stephan Ritter, Christian Nölleke, Carolin Hahn, Andreas Reiserer, Andreas Neuzner, Manuel Uphoff, Martin Mücke, Eden Figueroa, Joerg Bochmann, and Gerhard Rempe. An elementary quantum network of single atoms in optical cavities. *Nature*, 484(7393):195–200, 2012.

[10] Kyung Soo Choi, Hui Deng, Julien Laurat, and HJ Kimble. Mapping photonic entanglement into and out of a quantum memory. *Nature*, 452(7183):67–71, 2008.

[11] Adam T Black, James K Thompson, and Vladan Vuletić. On-demand superradiant conversion of atomic spin gratings into single photons with high efficiency. *Physical review letters*, 95(13):133601, 2005.

[12] S Sevinçli, N Henkel, C Ates, and T Pohl. Nonlocal nonlinear optics in cold rydberg gases. *Physical review letters*, 107(15):153001, 2011.

[13] Thibault Peyronel, Ofer Firstenberg, Qi-Yu Liang, Sebastian Hofferberth, Alexey V Gorshkov, Thomas Pohl, Mikhail D Lukin, and Vladan Vuletić. Quantum nonlinear optics with single photons enabled by strongly interacting atoms. *Nature*, 488(7409):57–60, 2012.

[14] Ofer Firstenberg, Thibault Peyronel, Qi-Yu Liang, Alexey V Gorshkov, Mikhail D Lukin, and Vladan Vuletić. Attractive photons in a quantum nonlinear medium. *Nature*, 2013.

[15] Christine Guerlin, Etienne Brion, Tilman Esslinger, and Klaus Mølmer. Cavity quantum electrodynamics with a rydberg-blocked atomic ensemble. *Physical Review A*, 82(5):053832, 2010.

[16] Valentina Parigi, Erwan Bimbard, Jovica Stanojevic, Andrew J. Hilliard, Florence Nogrette, Rosa Tualle-Brouri, Alexei Ourjoumtsev, and Philippe Grangier. Observation and measurement of interaction-induced dispersive optical nonlinearities in an ensemble of cold rydberg atoms. *Phys. Rev. Lett.*, 109:233602, Dec 2012.

[17] A Grankin, E Brion, E Bimbard, R Boddeda, I Usmani, A Ourjoumtsev, and P Grangier. Quantum statistics of light transmitted through an intracavity rydberg medium. *arXiv preprint arXiv:1312.2621*, 2013.

[18] Kyle Joseph Arnold. *Collective Dispersive Interaction of Atoms and Light in a High Finesse Cavity*. PhD thesis, National University of Singapore, 2012.

[19] Tobias Kampschulte. *Coherently driven three-level atoms in an optical cavity*. PhD thesis, Rheinische Friedrich-Wilhelms-Universiät Bonn, 2011.

[20] Daniel A. Steck. Quantum and atom optics. available online at `http://steck.us/teaching`.

[21] Surajit Sen, Mihir Ranjan Nath, Gautam Gangopadhyay, et al. Comparison of electromagnetically induced transparency in lambda, vee and cascade three-level systems. *arXiv preprint arXiv:1305.5056*, 2013.

[22] Jonathan D Pritchard. *Cooperative Optical Non-linearity in a blockaded Rydberg ensemble*. Springer, 2012.

[23] Jiepeng Zhang, Gessler Hernandez, and Yifu Zhu. Atomic coherence and interference in a coupled atom-cavity system. *Journal of Modern Optics*, 56(18-19):1955–1963, 2009.

[24] Daniel Comparat and Pierre Pillet. Dipole blockade in a cold rydberg atomic sample [invited]. *JOSA B*, 27(6):A208–A232, 2010.

[25] S Inouye, AP Chikkatur, DM Stamper-Kurn, J Stenger, DE Pritchard, and W Ketterle. Superradiant rayleigh scattering from a bose-einstein condensate. *Science*, 285(5427):571–574, 1999.

[26] Christopher J Foot. *Atomic physics*. Oxford University Press, 2004.

[27] Jean Dalibard and Claude Cohen-Tannoudji. Laser cooling below the doppler limit by polarization gradients: simple theoretical models. *JOSA B*, 6(11):2023–2045, 1989.

[28] Harold J Metcalf and Peter Van der Straten. *Laser cooling and trapping*. Springer, 1999.

[29] Rudolf Grimm, Matthias Weidemüller, and Yurii B Ovchinnikov. Optical dipole traps for neutral atoms. *arXiv preprint physics/9902072*, 1999.

[30] RWP Drever, John L Hall, FV Kowalski, J Hough, GM Ford, AJ Munley, and H Ward. Laser phase and frequency stabilization using an optical resonator. *Applied Physics B*, 31(2):97–105, 1983.

[31] Richard W Fox, Chris W Oates, and Leo W Hollberg. 1. stabilizing diode lasers to high-finesse cavities. *Cavity-Enhanced Spectroscopies. Series: Experimental Methods in the Physical Sciences, ISBN: 9780124759879. Elsevier, vol. 40, pp. 1-46*, 40:1–46, 2003.

[32] Firuz Torabi-Goudarzi and Erling Riis. Efficient cw high-power frequency doubling in periodically poled ktp. *Optics communications*, 227(4):389–403, 2003.

[33] Anthony A Tovar and Lee W Casperson. Generalized beam matrices: Gaussian beam propagation in misaligned complex optical systems. *JOSA A*, 12(7):1522–1533, 1995.

[34] W Ketterle, DS Durfee, and DM Stamper-Kurn. Making, probing and understanding bose-einstein condensates. *arXiv preprint cond-mat/9904034*, 5, 1999.